OUKA
The University of Osaka
Institutional Knowledge Archive

Title	Spatial Profiling Identified Senescent Cancer-Associated Fibroblasts Localized in the Border Region of Human Pancreatic Ductal Adenocarcinoma
Author(s)	Harada, Yoshiyuki; Masuda, Atsuhiro; Matsuura, Takanori et al.
Citation	Cellular and Molecular Gastroenterology and Hepatology. 2026, 20(8), p. 101808
Version Type	VoR
URL	https://hdl.handle.net/11094/106747
rights	This article is licensed under a Creative Commons Attribution-NonCommercial-NoDerivatives 4.0 International License.
Note	

The University of Osaka Institutional Knowledge Archive : OUKA

https://ir.library.osaka-u.ac.jp/

The University of Osaka

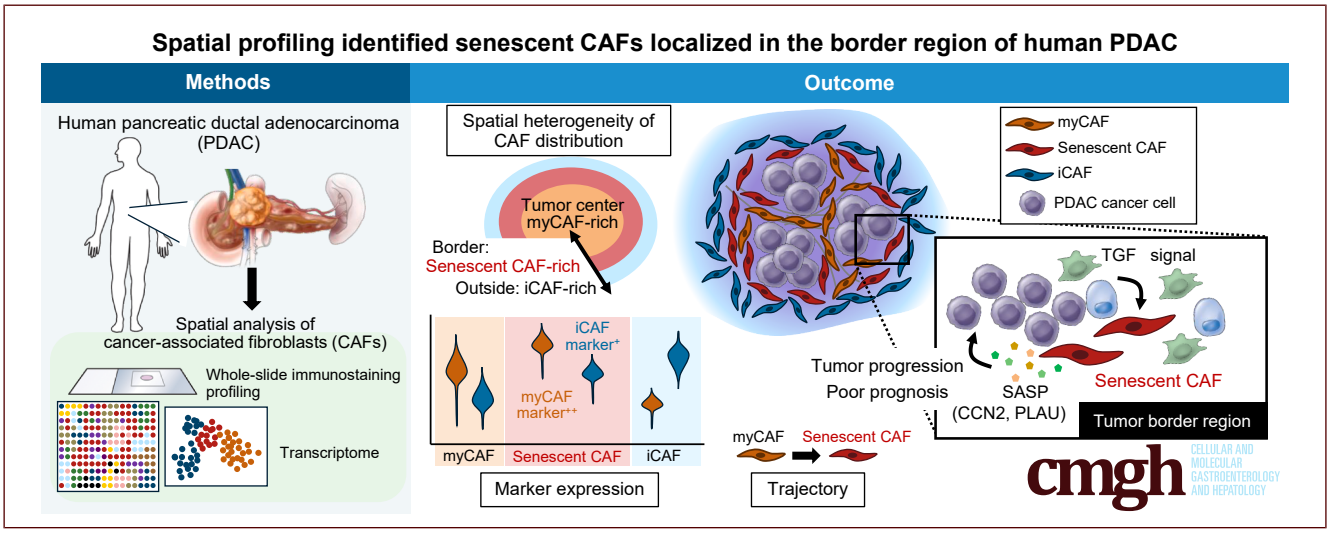
cmgh
CELLULAR AND MOLECULAR GASTROENTEROLOGY AND HEPATOLOGY

ORIGINAL RESEARCH

Spatial Profiling Identified Senescent Cancer-Associated Fibroblasts Localized in the Border Region of Human Pancreatic Ductal Adenocarcinoma

Yoshiyuki Harada,[1,2,3] Atsuhiro Masuda,[2] Takanori Matsuura,[1,2] Kenji Nagata,[1,2,3] Yoshihide Nanno,[4] Atsushi Masamune,[5] Yuzo Kodama,[2] Eiji Hara,[1,6] and Tomonori Matsumoto[1,3]

[1]*Department of Molecular Biology, Research Institute for Microbial Diseases, The University of Osaka, Osaka, Japan;* [2]*Division of Gastroenterology, Department of Internal Medicine, Graduate School of Medicine, Kobe University, Kobe, Japan;* [3]*Laboratory of Ploidy Pathology, Graduate School of Frontier Biosciences, The University of Osaka, Osaka, Japan;* [4]*Division of Hepato-Biliary-Pancreatic Surgery, Department of Surgery, Graduate School of Medicine, Kobe University, Kobe, Japan;* [5]*Division of Gastroenterology, Tohoku University Graduate School of Medicine, Sendai, Japan; and* [6]*Laboratory of Aging Biology, Immunology Frontier Research Center, The University of Osaka, Osaka, Japan*



SUMMARY

In human pancreatic ductal adenocarcinoma, senescent cancer-associated fibroblasts coexpress myofibroblastic and inflammatory cancer-associated fibroblast markers and preferentially localize at the gross tumor edge. Chemotherapy further induces this population, and senescent cancer-associated fibroblasts could influence disease progression through their senescence-associated secretory phenotype.

WHAT YOU NEED TO KNOW

Background: Pancreatic ductal adenocarcinoma contains abundant cancer-associated fibroblasts with diverse functions. Senescent cancer-associated fibroblasts, via a senescence-associated secretory phenotype, predict poor outcomes, yet their spatial dynamics remain undefined.

Impact: Immunostaining and spatial transcriptomics mapped fibroblast subpopulations across tumor regions. Senescent cancer-associated fibroblasts concentrate at the gross tumor edge, associate with poor survival, and expand after chemotherapy in myofibroblastic fibroblasts.

Future Directions: Eliminating senescent cancer-associated fibroblasts or suppressing their senescence-associated secretory phenotype may limit invasion. Transforming growth factor-β–axis molecules such as CCN2 and PLAU could serve as biomarkers and therapeutic targets to modulate stromal remodeling.

BACKGROUND & AIMS: Pancreatic ductal adenocarcinoma is a highly aggressive malignancy characterized by a fibroblast-rich tumor microenvironment. Cancer-associated fibroblasts closely interact with tumor cells and play a pivotal role in cancer pathogenesis. Single-cell analyses have identified distinct cancer-associated fibroblast subsets that exert either tumor-promoting or tumor-suppressive effects in pancreatic ductal adenocarcinoma. Senescent cancer-associated fibroblasts have recently been linked to poor prognosis through their senescence-associated secretory phenotype. However, the dynamics of senescent cancer-associated fibroblast induction and their spatial distribution in pancreatic ductal adenocarcinoma remain largely unclear. This study aimed to investigate the heterogeneity and spatial organization of cancer-associated fibroblasts in pancreatic ductal adenocarcinoma, with a specific focus on the induction and localization of senescent cancer-associated fibroblasts.

METHODS: We performed immunostaining and spatial transcriptomic analyses covering unbiased regions of tumor architecture to map cancer-associated fibroblast subpopulations and characterize senescent cancer-associated fibroblast induction and localization.

RESULTS: Senescent cancer-associated fibroblasts were found to accumulate preferentially at the gross tumor edge, and their abundance was associated with poor patient prognosis. Chemotherapy further promoted senescence in myofibroblastic cancer-associated fibroblasts within the tumor core, resulting in an increased population of senescent cancer-associated fibroblasts. Spatial transcriptomic profiling identified gene signatures specific to senescent cancer-associated fibroblasts and revealed their distinct interactions with neighboring cells. Notably, senescent cancer-associated fibroblasts exhibited enhanced transforming growth factor-β signaling activity and upregulation of downstream genes, such as CCN2 and PLAU, which may contribute to tumor proliferation and invasion.

CONCLUSIONS: This study reveals that senescent cancer-associated fibroblasts preferentially localize near the gross tumor edge and could impact tumor progression through their senescence-associated secretory phenotype. These findings highlight the spatial plasticity of pancreatic cancer-associated fibroblasts and underscore the pathological significance of senescent cancer-associated fibroblasts in human pancreatic ductal adenocarcinoma. *(Cell Mol Gastroenterol Hepatol 2026;20:101808; https://doi.org/10.1016/j.jcmgh.2026.101808)*

Keywords: Cellular Senescence; Pancreatic Cancer; Senescence-Associated Secretory Phenotype; Spatial Transcriptomics.

Pancreatic ductal adenocarcinoma (PDAC) is an aggressive malignancy with a particularly poor prognosis, which is characterized by the abundant accumulation of cancer-associated fibroblasts (CAFs) in its tumor microenvironment.[1–3] CAFs have been shown to influence cancer progression through diverse functions, including the production and remodeling of extracellular matrix components, secretion of soluble factors, and formation of specialized niches.[4,5] These activities contribute to multiple tumor-promoting processes, such as enhanced cancer cell proliferation and invasion, stimulation of angiogenesis, and suppression of antitumor immunity.[4,5] Based on their tumor-promoting roles, therapeutic strategies targeting CAFs have been explored.[4–6] However, some studies in mouse models have shown that CAF depletion accelerates pancreatic tumor progression,[7–9] highlighting their complex and context-dependent functions.

Recent advances in single-cell analysis technologies have revealed that CAFs consist of multiple subtypes with distinct characteristics.[4,5,10] The 2 most representative subtypes commonly observed across cancers are myofibroblastic CAFs (myCAFs) and inflammatory CAFs (iCAFs).[5,11] While myCAFs form the tumor stroma by producing and remodeling the extracellular matrix, iCAFs secrete inflammatory mediators that activate immune responses in the tumor microenvironment.[12] Notably, these CAF subtypes have also been reported to exhibit distinct spatial distributions, with myCAFs localized immediately adjacent to the cancer cells and iCAFs positioned more distantly from neoplastic cells,[11] implying that the characteristics and behavior of CAFs are strongly influenced by cancer cells within the tumor microenvironment. Moreover, given that cancers often invade surrounding tissues while forming solid masses and generate macroscopic heterogeneity within and around the tumor, it is necessary to analyze the heterogeneous characteristics of CAFs in relation to the overall tumor architecture.

Cellular senescence is a stress response characterized by irreversible cell cycle arrest and the secretion of various molecules known as senescence-associated secretory phenotypes (SASPs).[13–15] Although cellular senescence in damaged cells suppresses tumor initiation, senescent cells secrete various cytokines, growth factors, and matrix metalloproteinases as part of the SASP, which has been shown by our group and others to promote cancer development and progression.[14–17] Interestingly, cellular senescence has recently been identified in pancreatic CAFs, and previous studies have demonstrated their involvement in immune suppression and tumor progression in PDAC.[18–22] Therapeutic strategies targeting senescent cells are being actively investigated in diseases such as idiopathic pulmonary fibrosis,[14,23] and, given the tumor-promoting effects of senescent cells, such approaches are also expected to be promising in cancer therapy.[24–26] However, the SASP profile and functional impact of senescent cells vary

Abbreviations used in this paper: **αSMA, α smooth muscle actin; CAF, cancer-associated fibroblast; DPCAF, double-positive cancer-associated fibroblast; EVG, Elastica van Gieson; FFPE, formalin-fixed paraffin-embedded; GSEA, gene set enrichment analysis; iCAF, inflammatory cancer-associated fibroblast; IL, interleukin; myCAF, myofibroblastic cancer-associated fibroblast; PDAC, pancreatic ductal adenocarcinoma; SASP, senescence-associated secretory phenotype; TGFβ, transforming growth factor β.**

Most current article

© 2026 The Author(s). Published by Elsevier Inc. on behalf of American Gastroenterological Association Institute. This is an open access article under the CC BY-NC-ND license (http://creativecommons.org/licenses/by-nc-nd/4.0/).
2352-345X
https://doi.org/10.1016/j.jcmgh.2026.101808

considerably depending on the organ, cell type, and disease context,[13–15] and our understanding of how senescent CAFs contribute to PDAC pathogenesis remains limited.

In this study, we characterized the heterogeneity and spatial organization of pancreatic CAFs within the tumor architecture, with particular attention to senescent CAFs. Through unbiased analysis of tissue samples, including both tumor cores and surrounding regions, we revealed that senescent CAFs are preferentially localized at the gross tumor edge, and that tumors enriched in these cells are associated with a poor prognosis. Following chemotherapy, myCAFs located in the tumor core underwent cellular senescence, leading to an increased number of senescent CAFs. Spatial transcriptomic analysis identified genes specific to senescent CAFs and their interaction with other cellular components in different tumor regions. These findings indicate the novel plasticity of pancreatic CAFs and the implications of senescent CAFs in human PDAC.

Results

Characterization of Spatial Heterogeneity of Human Pancreatic Cancer-Associated Fibroblasts Identified Senescent Cancer-Associated Fibroblasts Near the Gross Tumor Edge

To analyze the spatial distribution and characteristics of CAFs in human pancreatic cancer, we first performed double immunohistochemical staining on surgically resected specimens using α smooth muscle actin (αSMA), a representative myCAF marker, and interleukin (IL)6, a representative iCAF marker. Analysis of 24 cases without preoperative chemotherapy revealed that αSMA-positive CAFs and IL6-positive CAFs were distributed in distinct regions within each case (Figure 1*A*). Interestingly, some CAFs were positive for both αSMA and IL6, and these double-positive CAFs were spatially localized within specific tumor areas. We categorized αSMA–single-positive CAFs as myCAFs, IL6–single-positive CAFs as iCAFs, and double-positive CAFs as DPCAFs, and examined their distribution patterns. Quantification of the area enriched with each CAF subtypes revealed that myCAFs were the most abundant subtype, whereas iCAFs and DPCAFs each accounted for approximately 20% of pancreatic CAFs (Figure 1*B*). Spatial analysis revealed that myCAFs were concentrated near the tumor center, iCAFs were biased toward areas outside the gross tumor edge, and DPCAFs were primarily distributed around the gross tumor edge. This distinct pattern showed that myCAFs, DPCAFs, and iCAFs occupy different regions from the tumor center to the periphery (Figure 1*C* and *D*). In particular, the mean distance of DPCAFs from the tumor center was 0.914 ± 0.162, which was close to the gross tumor edge, defined as 1 (Figure 1*D*; see Materials and Methods and the figure legend). These results suggest that DPCAFs, in addition to myCAFs and iCAFs, represent a unique CAF subtype with a distinct spatial distribution, being most abundant near the gross tumor edge.

Next, we investigated the characteristics of DPCAFs. Because recent studies have reported that some CAFs exhibit cellular senescence,[18,19] and IL6 is a key SASP factor,[14] we hypothesized that DPCAFs might represent senescent CAFs derived from αSMA–single-positive myCAFs. To test this, we assessed the expression of a cellular senescence marker p16 through immunostaining of serial sections. As expected, p16-positive CAFs were predominantly localized near the gross tumor edge, aligning with the distribution of DPCAFs (Figure 1*E*). Comparing p16 positivity rates among CAFs in regions enriched with myCAFs, iCAFs, and DPCAFs revealed that p16 positivity was low in myCAF- and iCAF-enriched regions but significantly higher in DPCAF-enriched regions (Figure 1*F*). Furthermore, CAFs in DPCAF-enriched areas were frequently positive for p21, another marker of cellular senescence, as well as γH2AX indicative of DNA damage, supporting their senescent characteristics (Figure 1*G*). These findings indicate that DPCAFs often exhibit features of cellular senescence and that senescent CAFs in human pancreatic cancer are double-positive for αSMA and IL6, predominantly localized near the gross tumor edge.

We further examined the relationship between CAF subset composition and clinical features. Notably, the proportion of DPCAFs within the CAF population was significantly higher in advanced cases (Figure 1*H*). There was also a trend toward an increased proportion of p16-positive CAFs with advancing clinical stages (Figure 1*I*). Comparing groups with high and low proportions of DPCAFs revealed a trend toward poorer recurrence-free survival in the high-DPCAF group (Figure 1*J*, Table 1). Similarly, the group with a higher proportion of p16-positive CAFs showed a trend toward worse prognosis compared with the group with fewer p16-positive CAFs (Figure 1*K*). Taken together, these findings highlight that CAF subsets in pancreatic cancer exhibit distinct spatial distributions, with DPCAFs displaying senescence features localized near the gross tumor edge, and their abundance correlating with tumor progression.

Chemotherapy Induces Double-Positive Cancer-Associated Fibroblasts With Senescence Features in Human Pancreatic Cancer

Next, we examined the heterogeneity and spatial distribution of CAFs in human pancreatic cancers treated with chemotherapy. Immunohistologic analysis revealed that tumors treated with intensive chemotherapy (see Materials and Methods) contained αSMA–single-positive myCAFs, IL6–single-positive iCAFs, and DPCAFs (Figure 2*A*). Notably, chemotherapy-treated tumors showed a significantly higher proportion of DPCAFs, which accounted for approximately 50% of the CAF population, compared with untreated tumors (Figure 2*B*). A comparison of CAF subset proportions revealed a significant increase in DPCAFs and a decrease in myCAFs in chemotherapy-treated tumors, whereas iCAF proportions remained unchanged regardless of chemotherapy history (Figure 2*B*). Spatial analysis showed that, as in untreated tumors, myCAFs and iCAFs in chemotherapy-treated tumors were predominantly localized near the tumor center and peripheral areas, respectively (Figure 2*C* and *D*). However, unlike untreated tumors, DPCAFs in chemotherapy-treated tumors were not only

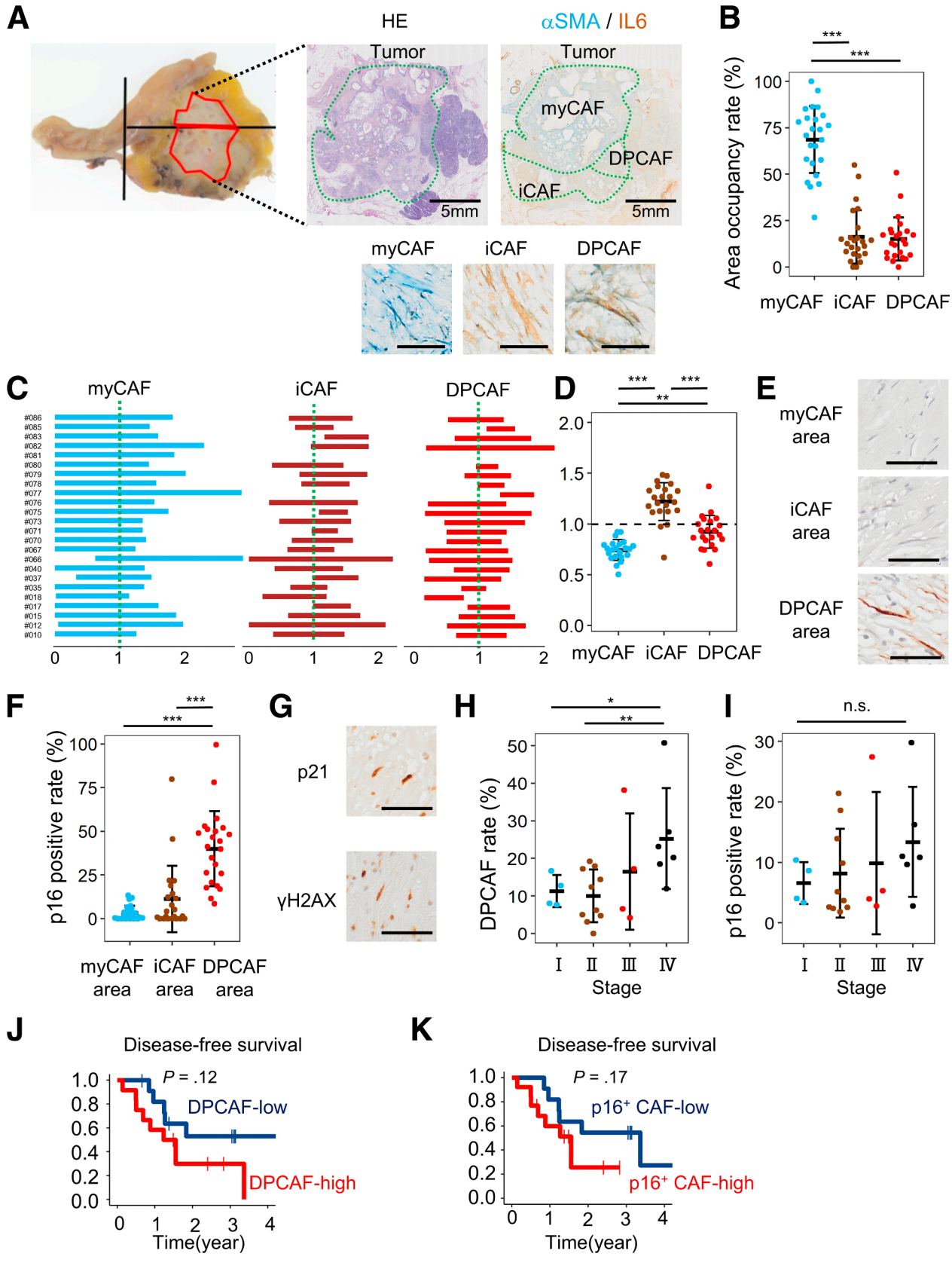

A
HE
αSMA / IL6
Tumor
Tumor
myCAF
DPCAF
iCAF
5mm
5mm
myCAF
iCAF
DPCAF
B
Area occupancy rate (%)
myCAF iCAF DPCAF
C
myCAF
iCAF
DPCAF
D
myCAF iCAF DPCAF
E
myCAF area
iCAF area
DPCAF area
F
p16 positive rate (%)
myCAF area
iCAF area
DPCAF area
G
p21
γH2AX
H
DPCAF rate (%)
Stage
I
n.s.
p16 positive rate (%)
Stage
J
Disease-free survival
P = .12
DPCAF-low
DPCAF-high
Time(year)
K
Disease-free survival
P = .17
p16+ CAF-low
p16+ CAF-high
Time(year)

Table 1. Clinical Information of Human PDAC Cases Without Chemotherapy

All patients (N = 24)	p16-high (n = 12)	p16-low (n = 12)	*P* value	DP-high (n = 12)	DP-low (n = 12)	*P* value
Age, *y*	69 (53–86)	68 (62–77)	1[a]	68 (53–86)	68 (62–82)	1[a]
Sex			.10[b]			1[b]
Male	3 (25)	8 (67)		6 (50)	5 (42)	
Female	9 (75)	4 (33)		6 (50)	7 (58)	
CEA, *ng/mL*	3.1 (0.4–5.8)	3.3 (1.3–9.3)	.51[a]	3.0 (1.3–9.3)	3.1 (0.4–7.9)	1[a]
CA19-9, *IU/mL*	120 (16–597)	85 (0–5978)	.95[a]	159 (16–1782)	59 (0–5978)	.18[a]
Differentiation			.49[d]			.17[c]
Well	3 (25)	5 (42)		3 (25)	5 (41)	
Moderate	8 (67)	6 (50)		7 (59)	7 (59)	
Poor	1 (8)	1 (8)		2 (16)	0 (0)	
Location			.14[c]			.14[d]
Head	10 (84)	10 (84)		10 (84)	10 (84)	
Body	0 (0)	2 (16)		2 (16)	0 (0)	
Tail	2 (16)	0 (0)		0 (0)	2 (16)	
Tumor diameter, *mm*	26 (15–41)	28 (17–47)	.69[a]	26 (15–41)	28 (17–47)	.71[a]
Pathologic stage						
I	2 (17)	2 (17)	.24[d]	1 (8)	3 (25)	.049[c]
II	4 (33)	6 (50)		4 (33)	6 (50)	
III	1 (8)	3 (25)		2 (17)	2 (17)	
IV	5 (42)	1 (8)		5 (42)	1 (8)	

NOTE. Cases were divided into 2 groups (high and low) based on the p16 positivity rate in CAFs. In addition, cases were also classified into high and low groups according to the abundance of DPCAF regions positive for both αSMA and IL6.
NOTE. Data are presented as number (%) or median (interquartile range).
αSMA, α smooth muscle actin; CAF, cancer-associated fibroblast; DPCAF, double-positive cancer-associated fibroblast; IL6, interleukin6; PDAC, pancreatic ductal adenocarcinoma.
[a]Mann–Whitney *U* test.
[b]Fisher's exact test.
[c]Cochran–Armitage trend test.
[d]χ^2 test.

concentrated near the gross tumor edge but also interspersed within regions rich in myCAFs near the tumor center (Figure 2*C*). These findings suggest that chemotherapy induces the transformation of myCAFs into DPCAFs.

We further investigated the cellular senescence features of pancreatic CAFs following chemotherapy. Immunostaining revealed that CAFs in DPCAF-predominant areas frequently expressed p16 in chemotherapy-treated tumors (Figure 2*E* and *F*). In contrast, CAFs in myCAF- and iCAF-predominant areas showed significantly lower p16 positivity, indicating that p16-positive CAFs largely correspond to DPCAFs (Figure 2*F*). Moreover, CAFs in areas predominant with p16-positive CAFs also expressed p21 and γH2AX, further confirming their senescence characteristics (Figure 2*G*). Quantification showed a significant increase in p16-positive CAFs after chemotherapy, suggesting that chemotherapy induces cellular senescence in CAFs (Figure 2*H*). This increase was more pronounced in patients treated with intensive chemotherapy regimens compared with those receiving less intensive regimens (see Materials and Methods), indicating that cellular damage from intensive chemotherapy drives therapy-induced senescence in CAFs (Figure 2*I*). Importantly, similar to patients without preoperative chemotherapy, those with higher proportions of p16-positive CAFs after preoperative chemotherapy exhibited significantly worse overall survival and disease-free survival compared with those with lower proportions of p16-positive CAFs (Figure 2*J* and *K*).

Figure 1. (***See previous page***). **Spatial characterization and prognostic impact of CAFs in PDAC without preoperative chemotherapy.** (*A*) Representative images of a PDAC tissue sample without preoperative chemotherapy. A macroscopic view, corresponding H&E-stained section, and αSMA/IL6 double-immunostained images are shown. *Dotted lines* indicate the gross tumor edge and the borders of myCAF-, iCAF-, and DPCAF-rich areas. (*B*) Proportions of myCAF-, iCAF-, and DPCAF-rich areas within the tumors. (*C*) Distribution of myCAF-, iCAF-, and DPCAF-rich areas within each tumor. (*D*) Normalized mean distance of each CAF subtype from the tumor center. In (*C*) and (*D*), the tumor center is defined as 0, and the gross tumor edge as 1. The spread of each area is represented by its relative distance from the tumor center. (*E*) Representative p16 immunostaining images of myCAF-, iCAF-, and DPCAF-rich areas. (*F*) Proportion of p16-positive CAFs within each CAF area. (*G*) Immunohistochemical staining for p21 and γH2AX in p16-positive CAF areas. (*H* and *I*) Proportion of DPCAFs and p16-positive CAFs stratified by tumor stage. In (*B*), (*D*), (*F*), (*H*), and (*I*), error bars indicate mean ± SD, and statistical differences were determined by Student's *t* test. $^*P < .05$, $^{**}P < .01$, $^{***}P < .001$. (*J* and *K*) Kaplan–Meier curves of disease-free survival, stratified by proportions of DPCAFs and p16-positive CAFs. Statistical differences were determined by the log-rank test. Scale bars, 50 μm. H&E, hematoxylin and eosin; SD, standard deviation.

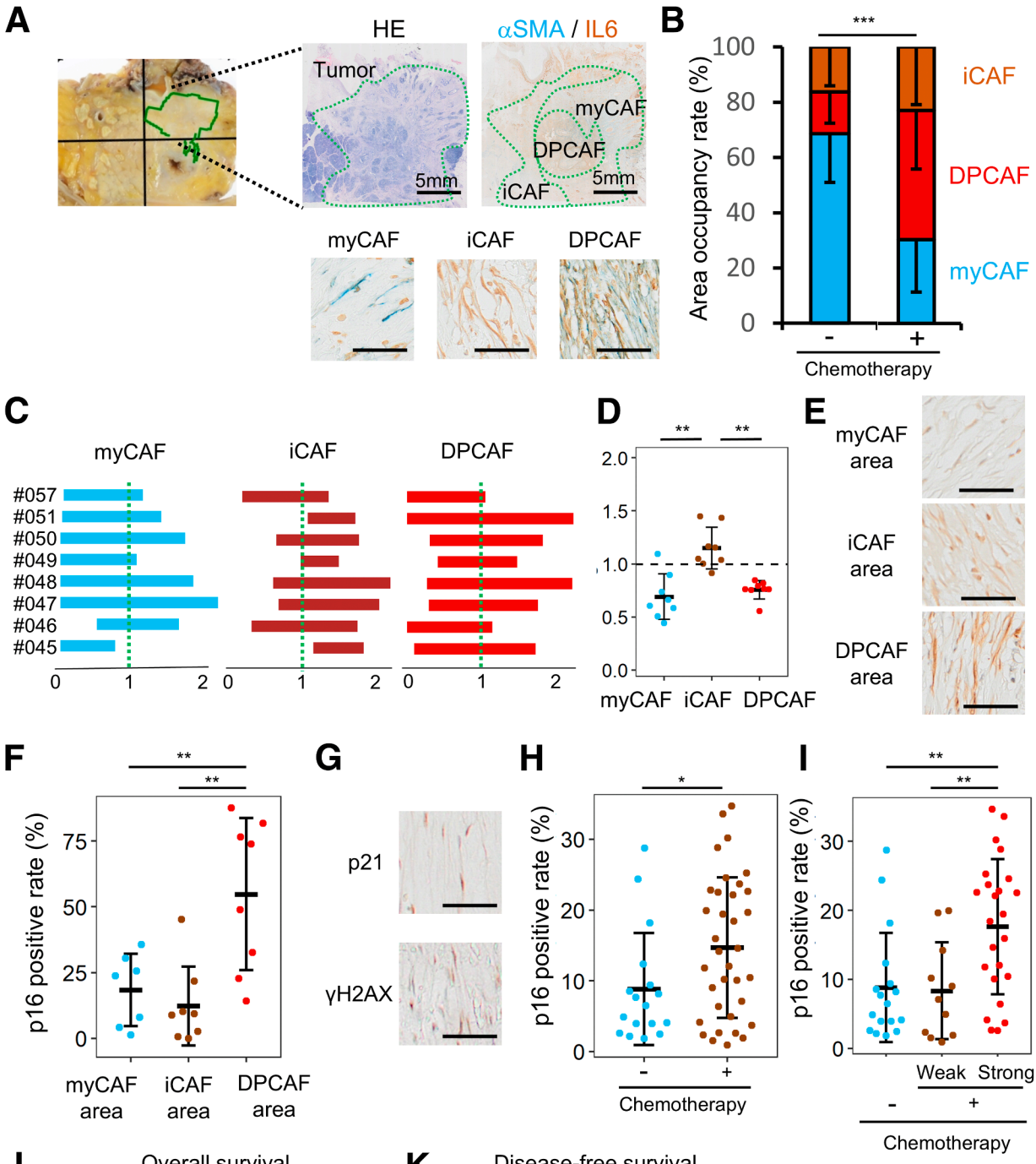

A
HE
αSMA / IL6
Tumor
5mm
myCAF
DPCAF
iCAF
myCAF
iCAF
DPCAF
B
***
Area occupancy rate (%)
iCAF
DPCAF
myCAF
Chemotherapy
C
myCAF
iCAF
DPCAF
#057
#051
#050
#049
#048
#047
#046
#045
D
**
**
myCAF iCAF DPCAF
E
myCAF area
iCAF area
DPCAF area
F
p16 positive rate (%)
myCAF area
iCAF area
DPCAF area
G
p21
γH2AX
H
*
p16 positive rate (%)
Chemotherapy
I
**
**
p16 positive rate (%)
Weak Strong
Chemotherapy
J
Overall survival
P = .0016
p16⁺ CAF-low
p16⁺ CAF-high
Time(year)
K
Disease-free survival
P = .0011
p16⁺ CAF-low
p16⁺ CAF-high
Time(year)

Table 2. Clinical Information of Human PDAC Cases After Chemotherapy

All patients (N = 36)	p16 high (n = 18)	p16 low (n = 18)	*P* value
Age, *y*	68 (47–80)	66 (27–79)	.49[a]
Sex			
Male	8 (44)	10 (56)	.74[b]
Female	10 (56)	8 (44)	
CEA, *ng/mL*	2 (1–7)	3 (1–8)	.23[a]
CA19-9, *IU/mL*	130 (1–2961)	863 (1–1653)	.42[a]
Differentiation			
Well	7 (39)	4 (22)	.25[c]
Moderate	10 (56)	12 (67)	
Poor	1 (6)	2 (11)	
Location			
Head	13 (72)	16 (88)	.44[d]
Body	2 (11)	1 (6)	
Tail	3 (17)	1 (6)	
Tumor diameter, *mm*	35 (20–90)	29 (7–44)	.013[a]
Pathologic stage			
I	2 (11)	2 (11)	.09[c]
II	9 (50)	14 (78)	
III	2 (11)	1 (6)	
IV	5 (28)	1 (6)	
Chemotherapy			
Weak	2	9	.028[d]
Strong	16	9	

NOTE. Cases were divided into 2 groups (high and low) based on the p16 positivity rate in CAFs.
NOTE. Data are presented as number (%) or median (interquartile range).
CAF, cancer-associated fibroblast; PDAC, pancreatic ductal adenocarcinoma.
[a]Mann–Whitney *U* test.
[b]Fisher's exact test.
[c]Cochran–Armitage trend test.
[d]χ^2 test.

Although differences in chemotherapy intensity between groups with high and low p16-positive CAF proportions (Table 2) complicate direct comparisons, these findings suggest that chemotherapy-induced senescence in CAFs may negatively impact postoperative prognosis, even in patients receiving preoperative chemotherapy.

Collectively, our results indicate that chemotherapy induces cellular senescence, especially in myCAFs, and that the abundance of senescent CAFs is linked to the clinical outcomes of pancreatic cancer.

Spatial Transcriptomic Analysis Confirmed the Senescence Phenotype of Double-Positive Cancer-Associated Fibroblasts and Clarified Their Distinct Gene Expression Profiles

To characterize the tumor microenvironment within regions enriched for each CAF subtype, we performed immunohistochemical analyses using serial sections from tumors without a history of chemotherapy. Staining for KRT7, a marker of tumor epithelial cells, showed that KRT7-positive tumor cells were significantly more

Figure 2. (***See previous page***). **Characteristics of CAFs in PDAC after preoperative chemotherapy.** (*A*) Representative images of a PDAC tissue sample after preoperative chemotherapy. A macroscopic view, corresponding H&E-stained section, and αSMA/IL6 double-immunostained images are shown. *Dotted lines* indicate the gross tumor edge and the borders of myCAF-, iCAF-, and DPCAF-rich areas. (*B*) Proportions of myCAF-, iCAF-, and DPCAF-rich areas with and without preoperative chemotherapy. (*C*) Distribution of myCAF-, iCAF-, and DPCAF-rich areas within each tumor after preoperative chemotherapy. (*D*) Normalized mean distance of each CAF subtype from the tumor center. In (*C*) and (*D*), the tumor center is defined as 0, and the gross tumor edge as 1. The spread of each area is represented by its relative distance from the tumor center. (*E*) Representative p16 immunostaining of myCAF-, iCAF-, and DPCAF-rich areas. (*F*) Proportion of p16-positive CAFs within each CAF area. (*G*) Immunohistochemical staining for p21 and γH2AX in p16-positive CAF areas. (*H* and *I*) Frequency of p16 positivity in CAFs with and without preoperative chemotherapy. In (*B*), (*D*), (*F*), (*H*), and (*I*), error bars indicate mean ± SD, and statistical differences were determined by Student's *t* test. $^*P < .05$, $^{**}P < .01$, $^{***}P < .001$. (*J* and *K*) Kaplan–Meier curves of overall survival and disease-free survival, stratified by proportion of p16-positive CAFs in cases with preoperative chemotherapy. Statistical differences were determined by the log-rank test. Scale bars, 50 μm. H&E, hematoxylin and eosin; SD, standard deviation.

abundant in myCAF-enriched regions and, to a lesser extent, in DPCAF-enriched regions, whereas they were markedly reduced in iCAF-enriched regions, supporting the observation that myCAFs localize in close proximity to the tumor center (Figure 3*A* and *B*). Elastica van Gieson (EVG) staining revealed a tendency toward a prominent collagen presence particularly within myCAF-enriched regions, which was consistent with the high collagen-producing capacity of myCAFs (Figure 3*A* and *B*). Analysis of tumor-infiltrating lymphocytes showed that CD8-positive T cells were most abundant in myCAF-enriched regions, whereas CD4-positive T cells showed no clear differences among regions (Figure 3*A* and *B*), and their numbers across all regions were comparable to previous reports describing pancreatic cancer as an immune-cold tumor.[27,28]

To further investigate the expression and spatial profiles of DPCAFs within tumors, spatial transcriptomic analysis using Visium was performed on 2 tumors without chemotherapy history. Analysis regions were selected to encompass the 3 CAF subsets (myCAF, iCAF, and DPCAF) identified through immunohistochemical staining in Figure 1. Integrated analysis of the 2 samples divided the Visium spots into 13 clusters (Figure 4*A*). Each cluster was annotated based on predominant cell types, determined by gene expression profiles and hematoxylin and eosin pathologic features. The 13 clusters were categorized into 5 types: fibroblast-rich, cancer cell-rich, acinar cell-rich, endothelial cell-rich, and undetermined (Figure 4*B* and *C*; Supplementary Table 1).

To further characterize pancreatic CAFs, we focused on 6 fibroblast-rich clusters (clusters 1, 3, 4, 5, 8, and 11) among the 13 identified clusters. Based on spatial distribution and gene expression profiles, clusters 3 and 4 were identified as iCAF-rich, clusters 1, 8, and 11 as myCAF-rich, and cluster 5 as DPCAF-rich (Figure 4*D*; Supplementary Table 1). Consistent with the immunohistochemical findings, both samples showed a spatial distribution where myCAF-rich clusters, DPCAF-rich clusters, and iCAF-rich clusters were sequentially arranged from the tumor center to the periphery (Figure 4*E*). Representative marker genes for myCAFs (ACTA2 and HOPX) and iCAFs (IL6 and HAS2) were highly expressed in myCAF-rich and iCAF-rich clusters, respectively (Figure 4*F*). Interestingly, DPCAFs exhibited stronger expression of myCAF markers compared with myCAFs, whereas iCAF markers were expressed less strongly than in iCAFs but significantly higher than in myCAFs (Figure 4*F* and *G*). These findings highlight the distinct characteristics of DPCAFs as a unique subset.

Gene set enrichment analysis (GSEA) was performed to examine the gene expression characteristics of the microenvironment in DPCAF-rich regions. Compared with both myCAF-rich and iCAF-rich clusters, DPCAF-rich clusters showed significantly higher expression of epithelial–mesenchymal transition-related genes, along with elevated expression trends in Notch signaling and the transforming growth factor β (TGFβ) pathway (Figure 5*A* and *B*; Supplementary Tables 2 and 3). Moreover, the gene set associated with cellular senescence was significantly enriched in DPCAF-rich clusters compared with the other 2 groups (Figure 5*C*). The senescent phenotype of DPCAFs was corroborated by enrichment of interferon-response gene sets and the p53 pathway in DPCAF-rich clusters relative to iCAFs (Supplementary Table 3). CDKN2A and CDKN2B, key genes associated with cellular senescence, were also expressed at the highest levels in DPCAF-rich clusters, further confirming that CAFs in these clusters exhibit cellular senescence features (Figure 5*D*). Differential expression analysis identified 253 genes with significantly elevated expression in DPCAF-rich clusters compared with both myCAF- and iCAF-rich clusters (Figure 5*E*; Supplementary Table 4). Among the 253 genes significantly upregulated in DPCAFs, 6 genes (CYP26A1, MATN3, RFLNA, RGS16, STMN2, and TIMP3) that were not included in myCAF or iCAF markers were identified as DPCAF-specific, based on their Log fold change values greater than 1.5 compared with both myCAFs and iCAFs, and their high expression levels in DPCAFs (Figure 5*F*). These 6 genes effectively distinguished DPCAFs from other CAF subsets (Figure 5*G*).

Taken together, spatial transcriptomic analysis confirmed the presence of a DPCAF population predominantly localized near the gross tumor edge, characterized by a gene expression profile distinct from both myCAFs and iCAFs. DPCAFs exhibited moderate iCAF-like features together with high expression of myCAF markers, uniquely expressed senescence-related genes, and other molecules identified as DPCAF-specific.

Transforming Growth Factor β Signaling Is Enhanced in the Double-Positive Cancer-Associated Fibroblast Microenvironment

We further sought to understand how DPCAF-rich regions communicate with the surrounding tumor environment. Pathway and gene ontology analyses of the 253 genes highly expressed in DPCAFs (Figure 5*E*; Supplementary Table 4) revealed that gene ontology terms related to the extracellular matrix, as well as genes associated with TGFβ signaling, were enriched among these genes (Supplementary Table 5). Intercellular communication analysis also identified strong TGFβ input into DPCAFs (Figure 6*A* and *B*). The sources of TGFβ signaling were widely distributed, including iCAFs, endothelial cells, and acinar cell–rich clusters located both inside and outside the tumor (Figure 6*A* and *B*). Consistently, the DPCAF-rich clusters exhibited increased expression of the TGFβ receptor TGFBR1, the TGFβ mediator LTBP2, and CCN2, a downstream effector that also amplifies TGFβ signaling (Figure 6*C*). Furthermore, PLAU, a gene regulated downstream of TGFβ, was also upregulated in the DPCAF-rich clusters, and PLAU signaling was observed to be broadly outputted from the DPCAF-rich areas into the surrounding tumor environment (Figure 6*A, D*, and *E*). These findings suggest that DPCAF-rich regions are strongly influenced by TGFβ signaling from the surrounding environment, and that PLAU signaling emanates from these regions to affect neighboring areas, highlighting intensive crosstalk between DPCAFs and the tumor microenvironment.

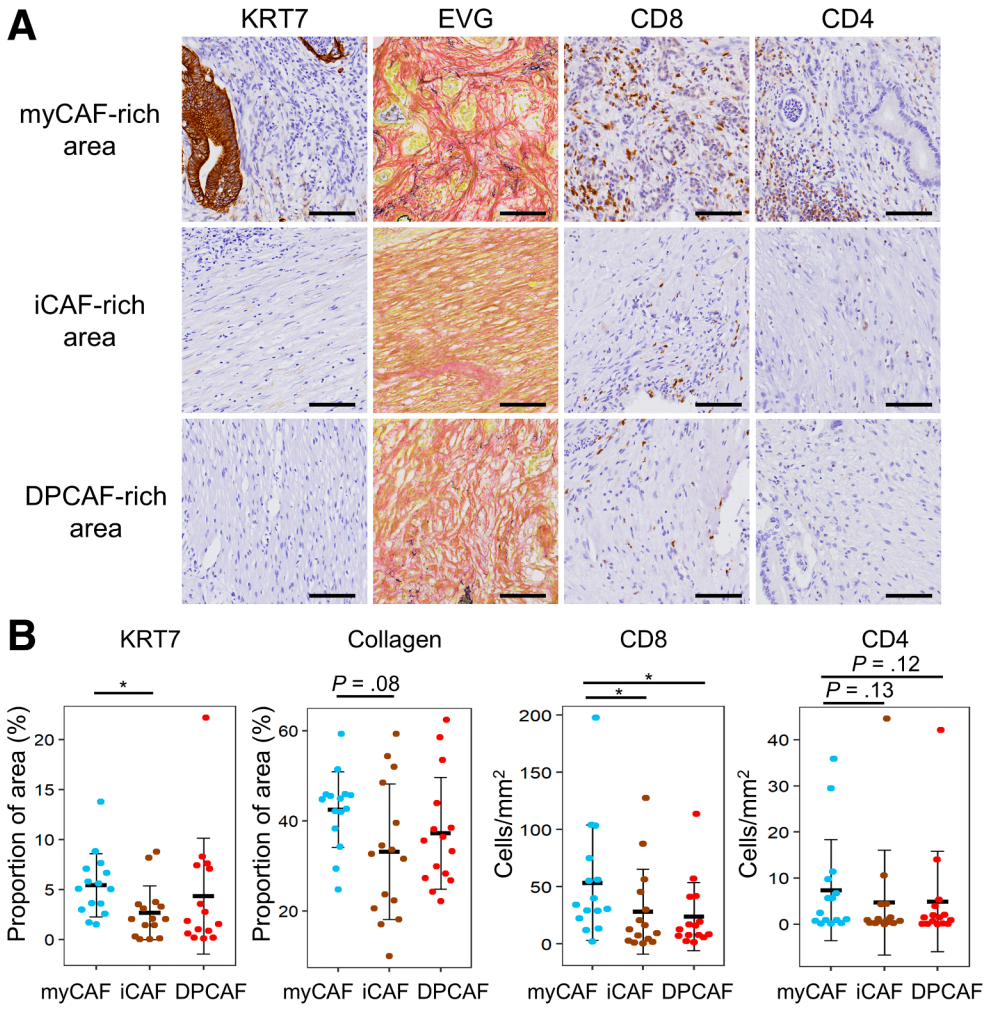


Figure 3. Immunohistochemical and EVG staining of PDACs without prior chemotherapy. (*A*) Representative immunohistochemical and EVG staining of myCAF-, iCAF-, and DPCAF-rich areas. Scale bars, 100 μm. (*B*) Quantitative analysis of immunohistochemical and EVG staining. *$P < .05$.

To further investigate the mechanism underlying the formation of DPCAF, we performed pseudotime analysis, which suggested a continuous trajectory of CAF transitions from the tumor center to the periphery, that is, from myCAF to iCAF, with DPCAF positioned in the middle of this progression (Figure 7*A*). Evaluation of CAF proliferation by Ki67 immunostaining showed that CAFs within myCAF-enriched regions had a significantly higher Ki67 positivity than those in DPCAF- or iCAF-enriched regions, further supporting the possibility that DPCAFs located at the gross tumor edge may originate from highly proliferative myCAFs that undergo proliferation-associated telomere shortening or other triggers that lead to cellular senescence (Figure 7*B* and *C*). Given that DPCAF expressed myCAF-related genes more strongly than myCAF itself, it can be hypothesized that DPCAF originates from myCAF under the influence of TGFβ signaling.

Chemotherapy Induces Cellular Senescence in Myofibroblastic Cancer-Associated Fibroblasts, Leading to Their Widespread Distribution Within Pancreatic Ductal Adenocarcinoma Tumors

Next, we performed spatial transcriptomic analysis on 2 cases treated with preoperative chemotherapy. Similar to the cases without preoperative chemotherapy, integrated analysis classified the Visium spots into 12 clusters, with clusters 0, 5, 6, and 11 identified as fibroblast-rich clusters (Figure 8*A* and *B*). These fibroblast-rich clusters were further examined by reclustering after selection, which identified 5 subclusters (Figure 8*C* and *D*). Examination of myCAF and iCAF marker expression revealed that cluster CAF4 exclusively overexpressed iCAF markers while showing lower expression of myCAF markers, suggesting that CAF4 represents an iCAF-rich cluster (Figure 8*E*). The predominant localization of CAF4 at the tumor periphery, corresponding to the iCAF distribution observed in immunostaining, further supported the iCAF predominance in the CAF4 cluster (Figure 8*D*). In contrast, the remaining 4 clusters did not exhibit clear differences in the expression of myCAF and iCAF markers, making it difficult to define their characteristics. Of note, DPCAF markers identified in cases without preoperative chemotherapy were highly expressed in the CAF5 cluster (Figure 8*F* and *G*). Furthermore, although CAF1 to CAF3 clusters showed moderate levels of myCAF marker expression and lower levels of iCAF marker expression, with a slight inverse correlation between the 2, CAF5 demonstrated the highest expression of myCAF markers along with relatively high iCAF marker

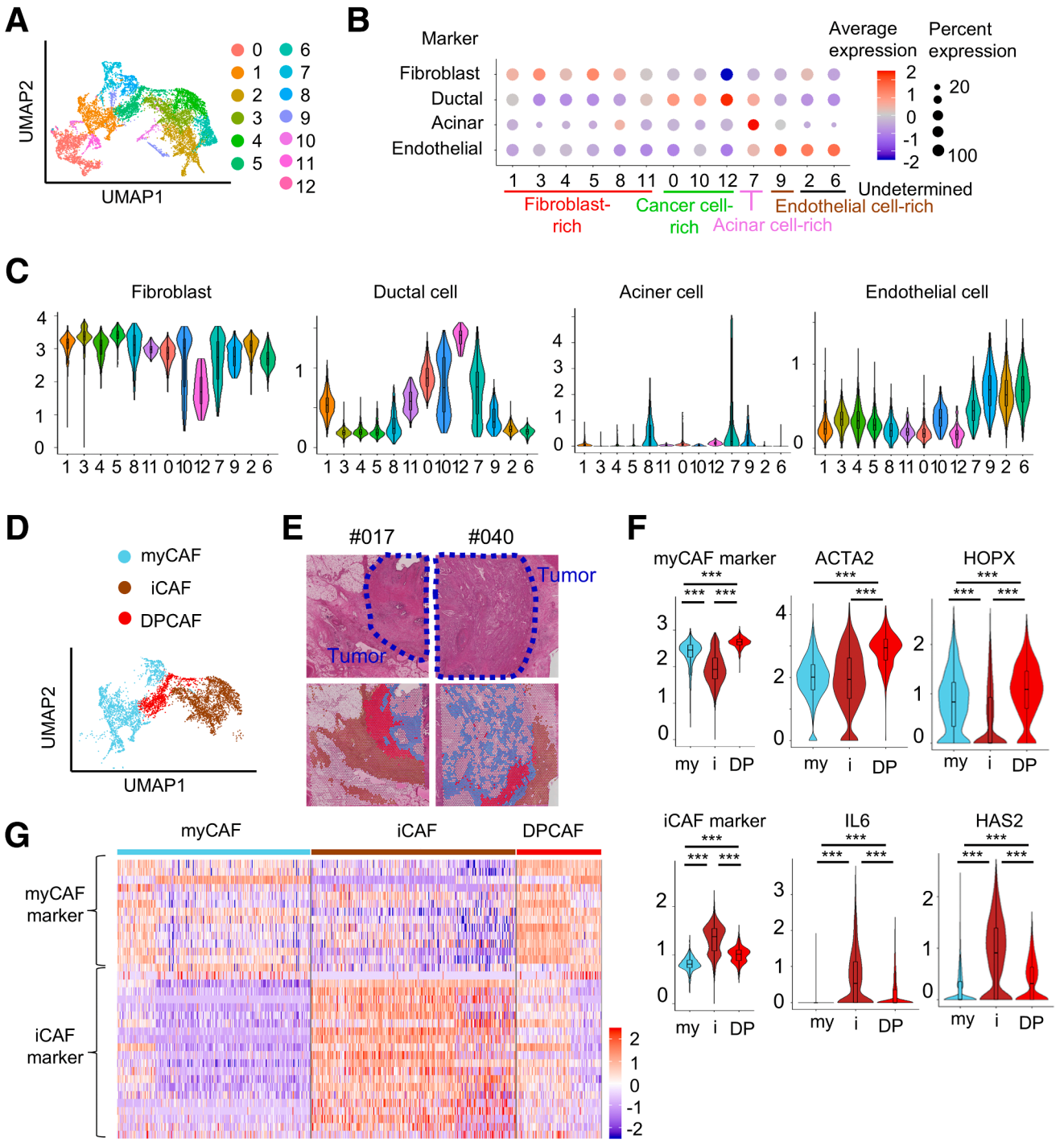


Figure 4. Spatial transcriptomic analysis of PDACs without chemotherapy. (*A*) UMAP clustering of analyzed spots. The results represent the integrated analysis of 2 cases. (*B*) Annotation of each cluster based on cell type markers. (*C*) Expression of cell type markers across all clusters. (*D*) UMAP plot showing only the CAF clusters. myCAFs (clusters 1, 8, 11), iCAFs (clusters 3, 4), and DPCAFs (cluster 5) were identified and color-coded according to gene expression patterns and comparison with H&E staining. (*E*) Spatial distribution of each CAF cluster. (*F* and *G*) Violin plots (*F*) and heatmap (*G*) showing the expression levels of myCAF and iCAF markers in each CAF cluster. Student's *t*-test. ***$P < .001$. H&E, hematoxylin and eosin; UMAP, Uniform Manifold Approximation and Projection.

expression among clusters other than CAF4 (Figure 8*E* and *F*). This expression pattern in the CAF5 cluster closely resembles that of DPCAFs observed in cases without preoperative chemotherapy (Figure 4*G*). These findings indicate that CAF5 is a DPCAF-rich cluster, whereas CAF1 to CAF3 are likely myCAF-rich clusters.

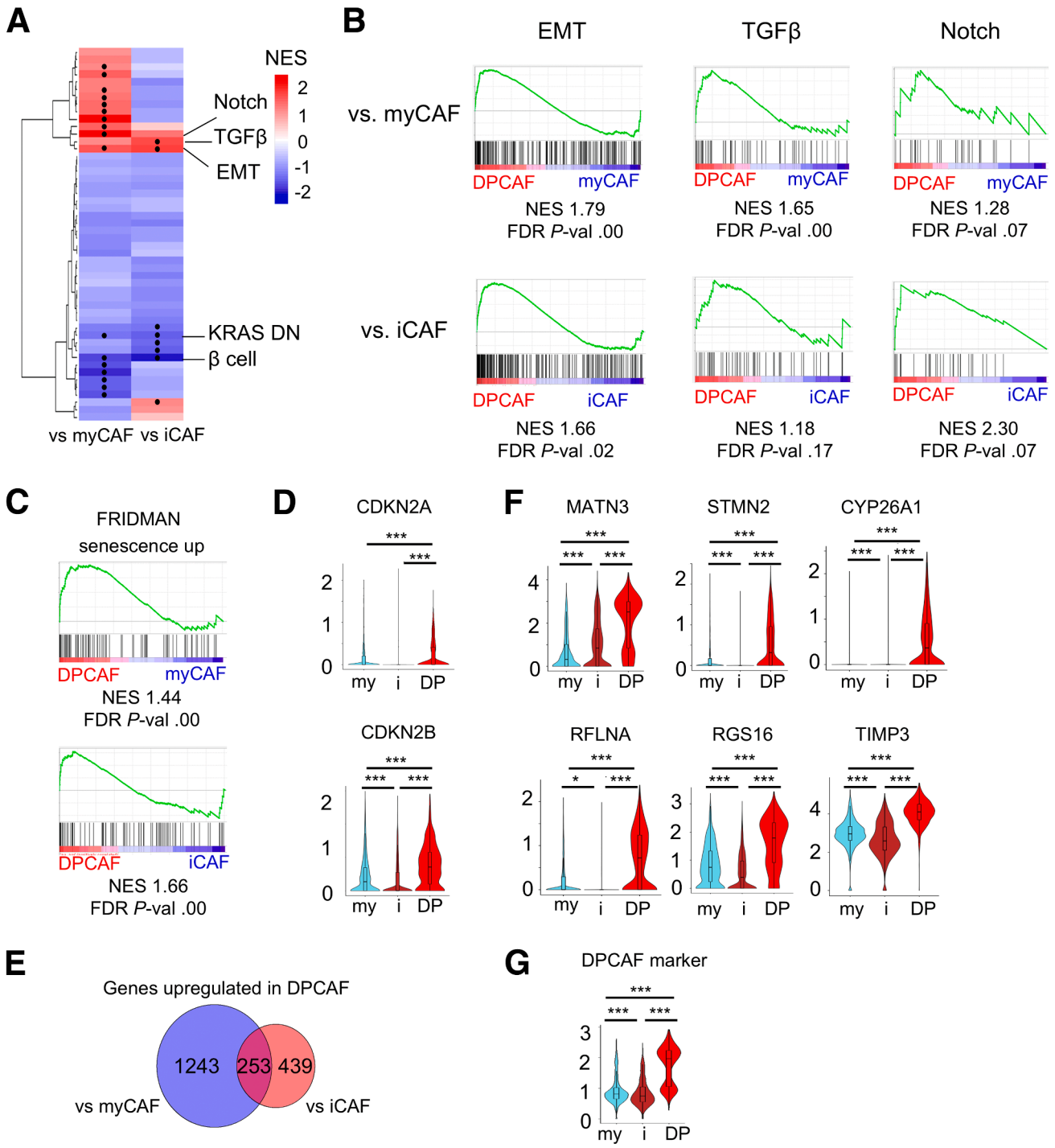
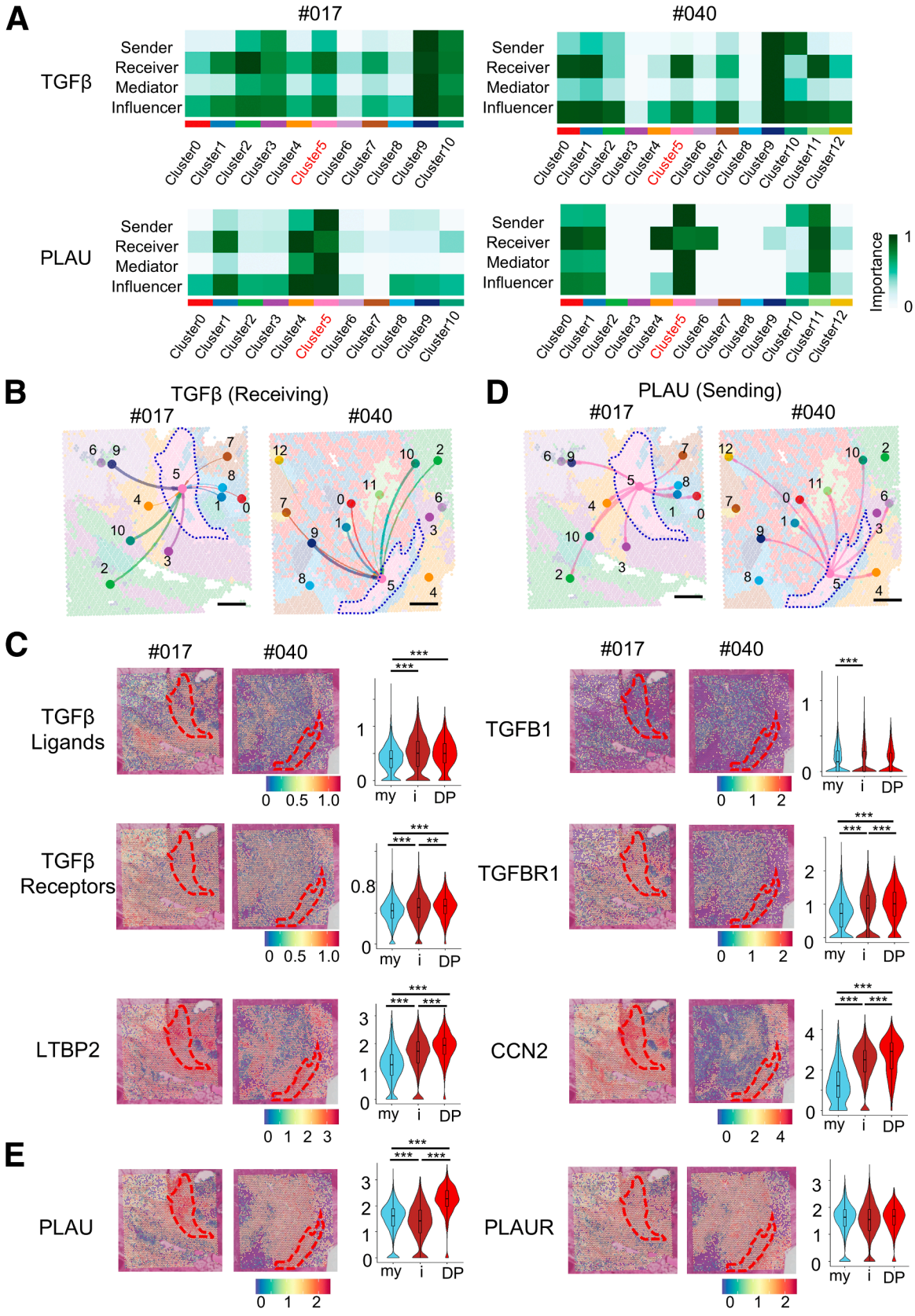


Figure 5. Gene expression profiles of CAF clusters identified by spatial transcriptomic analysis of PDACs without prior chemotherapy. (*A*) GSEA illustrating the gene expression characteristics of DPCAFs, compared with myCAFs and iCAFs, respectively. The *dots* indicate statistically significant changes with $P < .05$. (*B*) Plots of gene sets that showed significant enrichment in the GSEA. (*C*) Gene set enrichment plot of the FRIDMAN senescence gene set. (*D, F,* and *G*) Violin plots showing gene expression in each CAF cluster. Student's *t* test. $^{*}P < .05$, $^{**}P < .01$, $^{***}P < .001$. (*E*) Venn diagram showing genes significantly upregulated in DPCAFs compared with myCAFs and iCAFs. LogFC > 0.5 and *P* value < .05 were considered significant. FC, fold change; FDR, false discovery rate; NES, normalized enrichment score.

GSEA revealed that CAF5 showed higher expression of several pathways, including Notch and TGFβ signaling, compared with the myCAF-rich clusters CAF1 to CAF3 and the iCAF-rich cluster CAF4 (Figure 9*A*). In addition, the gene set associated with cellular senescence was significantly enriched in CAF5 compared with the other groups


A
#017
#040
TGFβ
PLAU
Sender
Receiver
Mediator
Influencer
Importance
B
TGFβ (Receiving)
D
PLAU (Sending)
C
TGFβ Ligands
TGFB1
TGFβ Receptors
TGFBR1
LTBP2
CCN2
E
PLAU
PLAUR
my
i
DP

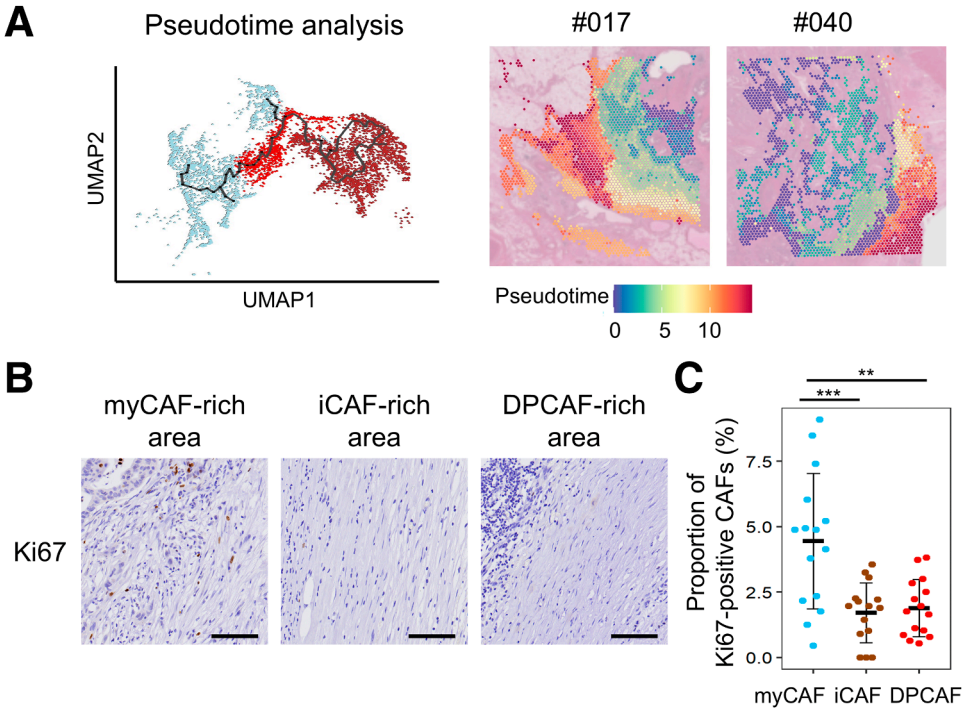


Figure 7. Pseudotime trajectory and proliferative activity of CAF subtypes. (*A*) Pseudotime analysis of CAF-rich clusters. (*B*) Representative Ki67 immunostaining images of myCAF-, iCAF-, and DPCAF-rich areas. (*C*) Proportion of Ki67-positive CAFs in each CAF area. Scale bars, 100 μm.

(Figure 9*B*). Consistent with this observation, CDKN2B was significantly upregulated in CAF5, whereas CDKN2A expression was detected only at low levels and was difficult to assess (Figure 9*C*). Pseudotime analysis demonstrated that CAF5 shared multiple trajectories with CAF1 to CAF3, whereas CAF4, corresponding to iCAFs, followed an independent trajectory (Figure 9*D*). These results suggest that chemotherapy primarily induces DPCAF from myCAF, similar to cases without prior chemotherapy. Taken together, spatial transcriptomic analyses indicate that chemotherapy-induced DPCAFs share gene expression features with DPCAFs observed in nonchemotherapy cases, although their spatial distributions differ.

Further Characterization of Senescent Cancer-Associated Fibroblasts In Vitro and in Human Pancreatic Ductal Adenocarcinoma

Next, we sought to validate the characteristics of DPCAF identified in the above analyses. Two pancreatic cancer–derived myCAF cell lines were treated with cisplatin to induce cellular senescence. Quantitative reverse transcription polymerase chain reaction analysis demonstrated increased expression of the senescence markers p16, p21, and IL6, as well as high expression of CCN2 and PLAU in senescent CAFs (Figure 10*A*). Furthermore, immunohistochemical staining of PLAU in several PDAC tissues from chemotherapy-naïve patients revealed strong PLAU expression in stromal cells located within DPCAF-rich areas near the gross tumor edge (Figure 10*B*).

To further examine the characteristics of DPCAF at single-cell resolution, subcellular spatial gene expression analysis (Xenium) was performed on 2 cases without prior chemotherapy. Overall, the expression patterns of ACTA2 and IL6 were consistent with the immunohistochemistry results. As expected, vimentin-positive CAFs within the DPCAF-rich regions coexpressed both ACTA2 and IL6 markers (Figure 11*A* and *B*). Importantly, the CDKN2A gene encodes 3 proteins, p16 and p14ARF, via distinct transcript variants that do not share a reading frame. Consequently, probes targeting exons common to both cannot accurately reflect p16 expression. To address this, we designed a custom probe to distinguish p16 from p14ARF in addition to the pre-existing CDKN2A probe included in the panel. Using this approach, we confirmed that DPCAF expresses p16, whereas KRT7-positive cells with CDKN2A signals

Figure 6. (***See previous page***). **Cell–cell communication analysis using spatial transcriptomic data.** (*A*) Heatmaps of TGFβ and PLAU pathway signaling analyzed using CellChat. Sender, receiver, mediator, and influencer were defined based on CellChat network centrality analysis of inferred cell–cell communication. See Materials and Methods for details. Clusters were annotated based on marker gene expression (Figure 4*B*) as follows: fibroblast-rich (Clusters 1, 3, 4, 5, 8, and 11), cancer cell-rich (Clusters 0, 10, and 12), acinar cell-rich (Cluster 7), endothelial cell-rich (Cluster 9), and undetermined (Clusters 2 and 6). (*B* and *D*) Spatial visualization of TGFβ (*B*) and PLAU (*D*) pathway signals received by DPCAF (cluster 5). Scale bars, 1 mm. (*C*) Spatial distribution of TGFβ signaling–related molecules and their differences among CAF clusters. The combined expression of TGFβ ligands and receptors, as well as several individual genes, is shown. (*E*) Spatial distribution of PLAU and PLAUR expression and their differences among CAF clusters. Student's *t* test. ***$P < .001$.

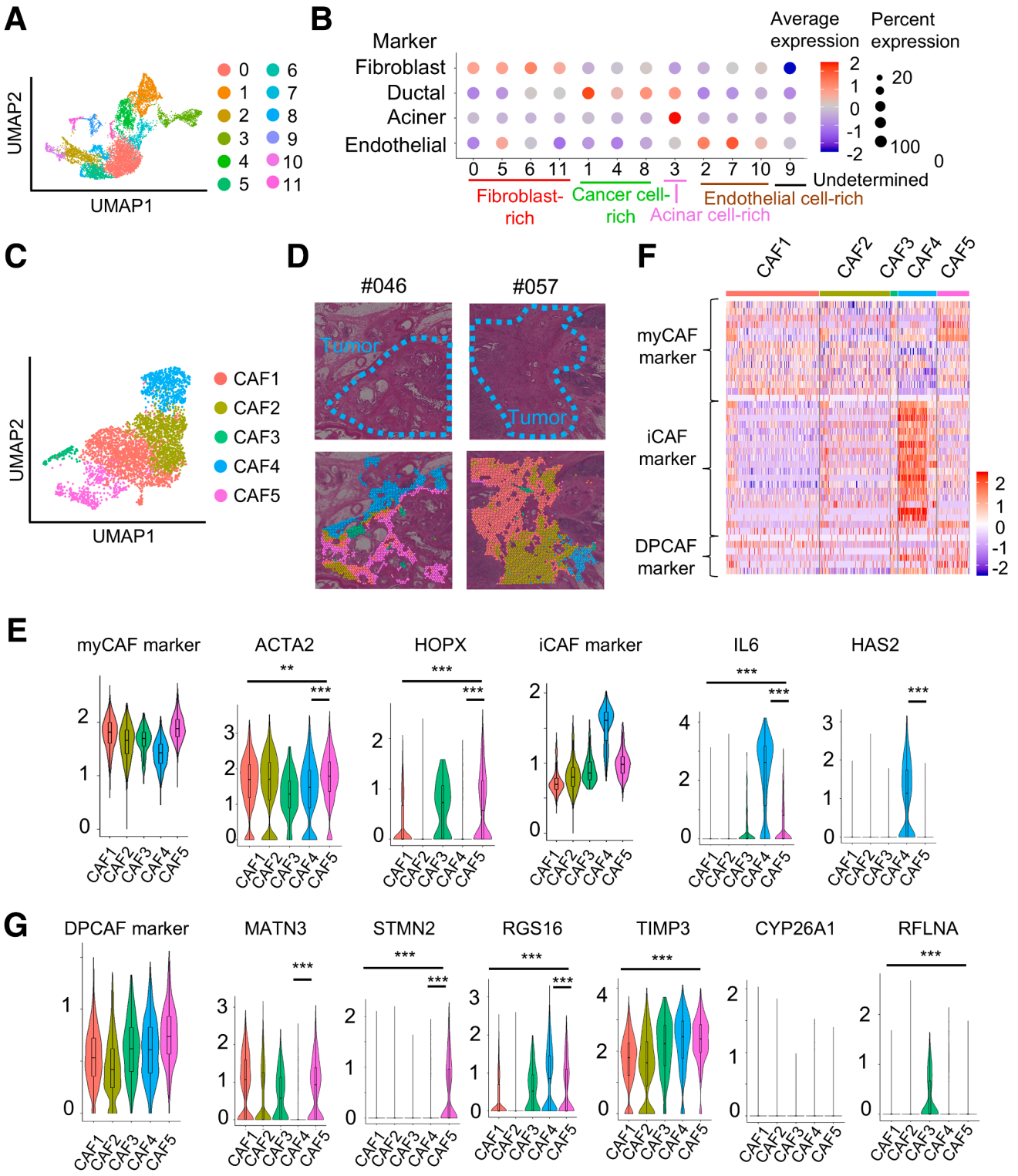


Figure 8. Spatial transcriptomic analysis of PDACs after chemotherapy. (*A*) UMAP clustering of analyzed spots. The results represent the integrated analysis of 2 cases. (*B*) Annotation of each cluster based on cell type markers. (*C*) UMAP plot highlighting CAF-rich spots. Reclustering was performed after selecting CAF-rich spots (clusters 0, 5, 6, and 11). (*D*) Spatial distribution of each CAF cluster. (*E, F,* and *G*) Violin plots (*E* and *G*) and heatmap (*F*) showing the expression levels of CAF markers. Student's *t* test. $^{*}P < .05$, $^{**}P < .01$, $^{***}P < .001$. UMAP, Uniform Manifold Approximation and Projection.

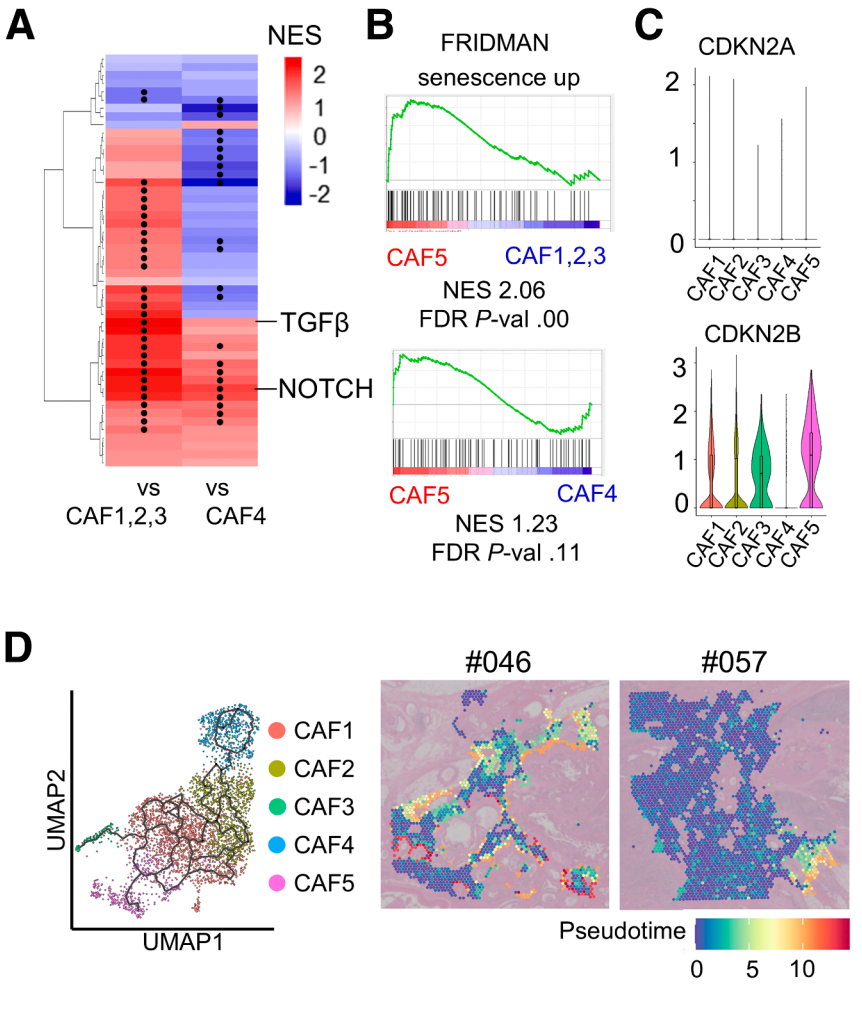


Figure 9. Gene set enrichment and pseudotime analysis of spatial transcriptomic data from PDACs after chemotherapy. (*A*) Gene set enrichment analysis demonstrating the gene expression characteristics of DPCAFs (CAF5) compared with myCAFs (CAF1, 2, and 3) and iCAFs (CAF4). The dots indicate statistically significant changes with $P <$ .05. (*B*) Gene set enrichment plot of the FRIDMAN senescence gene set. (*C*) Violin plots showing gene expression across CAF clusters. (*D*) Pseudotime analysis of CAF-rich clusters. FDR, false discovery rate; NES, normalized enrichment score.

were found to express primarily p14ARF rather than p16 (Figure 11*A*–*C*). Furthermore, DPCAF also showed strong expression of CDKN2B as well as MATN3 and RGS16, which were among the DPCAF markers identified in the Visium analysis (Figure 11*A* and *B*). These results validate the characteristics of DPCAF observed in the Visium analysis, confirming that DPCAF located near the gross tumor edge exhibits senescent phenotypes and that genes highly expressed in DPCAF-rich clusters represent the distinctive gene expression profile of DPCAF.

Discussion

In this study, we analyzed CAF heterogeneity and spatial localization in PDAC by evaluating tumor regions that evenly covered both the center and periphery without bias. We found macroscopically distinct spatial distributions of myCAFs and iCAFs throughout the tumor and showed that senescent CAFs were predominantly located at the gross tumor edge. The distinct spatial distributions of myCAFs and iCAFs observed in this study align with the previous study showing that myCAFs are microscopically located immediately adjacent to cancer cells, whereas iCAFs are positioned farther away, reflecting differences in their distance from tumor cells and the extent of tumor-derived influence.[11] Although some myCAFs in the tumor center did not appear directly adjacent to cancer cells, this may partly reflect the limitation of analyzing 2-dimensional tissue sections in our study. Nevertheless, compared with iCAFs, myCAFs are consistently located closer to tumor cells within the tumor mass, suggesting a stronger association with tumor cells. In contrast, our observation that senescent CAFs are predominantly located at the gross tumor edge appears inconsistent with the previous report describing their periductal localization closer to tumor cells than myCAFs.[19] Regions with high tumor cell content are often selected for analysis in cancer research, and such sampling bias may underlie inconsistent results. Our findings underscore the importance of analyzing CAFs across the entire tumor, including the periphery and surrounding tissue, particularly in PDAC, where CAFs exhibit macroscopically biased spatial distributions.

Because gene expression profiles associated with cellular senescence vary across tissues and cell lineages, cellular senescence is best evaluated using a combination of multiple markers.[13,29] We demonstrated that DPCAF

represents a senescent CAF population characterized by high expression of p16, CDKN2B, and senescence-related gene sets.[30] The higher expression of myCAF marker genes in DPCAF than myCAF itself, as well as pseudotime analysis and spatial distribution, supported that senescent CAF is likely derived from myCAF, consistent with a previous report.[19] The abundant TGFβ signaling input from both inside and outside the tumor into DPCAFs highlighted the involvement of TGFβ signaling in the induction of cellular senescence in pancreatic CAFs. Consistent with this finding, CDKN2B expression, a key mediator of TGFβ-induced cell-cycle arrest,[31] was markedly elevated in DPCAFs (Figures 3*I* and 7*A*). Furthermore, the distribution of senescent CAFs localized at the gross tumor edge implies that myCAFs generated within the tumor core may be pushed outward as the PDAC progresses and subsequently undergo cellular senescence, possibly upon receiving stimuli from the tumor exterior. Further investigation is warranted to elucidate the mechanisms underlying the induction of senescent CAFs in PDAC.

Notably, among PDAC cases without preoperative chemotherapy, tumors with abundant DPCAFs or p16-positive CAFs tended to exhibit poorer prognosis than those with lower levels. A similar association between DPCAF abundance and poor prognosis was observed in chemotherapy-treated cases, although it may have been influenced by certain biases in clinical background. The link between senescent CAFs and tumor progression or poor prognosis has also been consistently reported in PDAC and other cancers.[18–21,26] Interestingly, we identified CCN2 and PLAU, both downstream targets of TGFβ signaling,[32,33] as genes highly expressed in senescent DPCAFs. CCN2 is known to promote tumor cell proliferation,[34] whereas PLAU is a stromal-secreted factor that enhances tumor growth and invasion.[20] In a single-cell RNA sequencing atlas of PDAC integrating multiple datasets, tumor cells were shown to receive numerous signals from CAFs, including PLAU, with this cell–cell communication being the strongest within PDAC.[35] The localized distribution of senescent CAFs at the tumor front raises the possibility that DPCAFs may actively contribute to tumor expansion and progression through the secretion of these factors. Given the potential role of DPCAFs in tumor aggressiveness and the poor prognosis of PDAC, detecting DPCAFs could serve as a prognostic biomarker, and targeting them may provide a promising therapeutic strategy.

In conclusion, we revealed the characteristic spatial distribution, dynamics, and gene expression profiles of senescent CAFs in PDAC. Senescent CAFs are not merely bystanders arising from cellular damage but potentially promote tumor aggressiveness through the secretion of various factors. Although multiple CAF subsets, such as antigen-presenting CAFs,[36,37] Meflin-positive CAFs,[38] and periostin-positive CAFs,[39] have been reported in PDAC, senescent CAFs may constitute one of the key subsets amenable to therapeutic targeting. Further elucidating their molecular characteristics in PDAC could open new avenues for novel PDAC treatments.

Materials and Methods

Clinical Samples and Data

A total of 60 PDAC tissue samples were obtained from patients who underwent pancreatic resection between 2011 and 2022 at Kobe University Hospital in Kobe, Japan. Of the 60 patients, 24 had not received preoperative chemotherapy, whereas 36 had undergone preoperative chemotherapy. Among the 36 treated patients, the 25 who received modified folinic acid, fluorouracil, irinotecan hydrochloride, and oxaliplatin (FOLFIRINOX) or gemcitabine plus nab-paclitaxel were classified as the intensive chemotherapy group, whereas the 11 who received gemcitabine plus S-1, gemcitabine monotherapy, or S-1 monotherapy were classified as the less intensive chemotherapy group. Clinical data were obtained from the patients' medical records. This study was conducted in accordance with the Declaration of Helsinki and approved by the Ethics Committee of Kobe University School of Medicine. Opt-out consent was obtained because of the retrospective nature of the study.

Hematoxylin and Eosin Staining and Immunostaining

PDAC specimens were resected with an adequate resection margin beyond the gross tumor edge. After macroscopic photographs were taken, each specimen was divided into multiple formalin-fixed paraffin-embedded (FFPE) tissue blocks for embedding. With reference to the macroscopic images of the surgical specimen, we selected a representative FFPE block that contained a continuous region extending from the tumor center beyond the gross tumor edge into the extratumoral area. The selected FFPE tissues were sectioned at 5-μm thickness and stained with hematoxylin (Sakura 3G, Sakura Finetek) and eosin (1% Eosin Y solution, Muto Pure Chemicals) or processed for immunostaining. Immunohistochemistry was performed using primary antibodies against p16 (1:100, sc-56330, Santa Cruz), p21 (1:200, #2947, Cell Signaling), CD8 (1:150, M7103, Agilent Dako), CD4 (1:200, NCL-L-CD4-368, Leica), Ki67 (1:200, ab16667, Abcam), KRT7 (1:1000, M7018, Agilent Dako), and γH2A.X (1:4000, ab11174, Abcam), as well as secondary antibodies, including anti-rabbit (MP-7401, Vector Laboratories) and anti-mouse (MP-7402, Vector Laboratories) antibodies. For double immunostaining, the primary antibodies used were anti-IL6 (1:1000, ab9324, Abcam) and anti-αSMA (1:1000, ab124964, Abcam). The corresponding secondary antibodies were anti-mouse (MP-7402, Vector Laboratories) and anti-rabbit (MP-7401, Vector Laboratories) antibodies. The signals were detected using ImmPACT DAB (SK-4105, Vector Laboratories) and Vector Blue (SK-5300, Vector Laboratories) substrates. For the evaluation of collagen fibers, EVG staining was performed using Maeda-modified resorcin-fuchsin solution (Muto Pure Chemicals), Sirius Red (FUJIFILM Wako Pure Chemical Corporation), and Van Gieson solution P (FUJIFILM Wako Pure Chemical Corporation). The stained slides were scanned to generate whole-

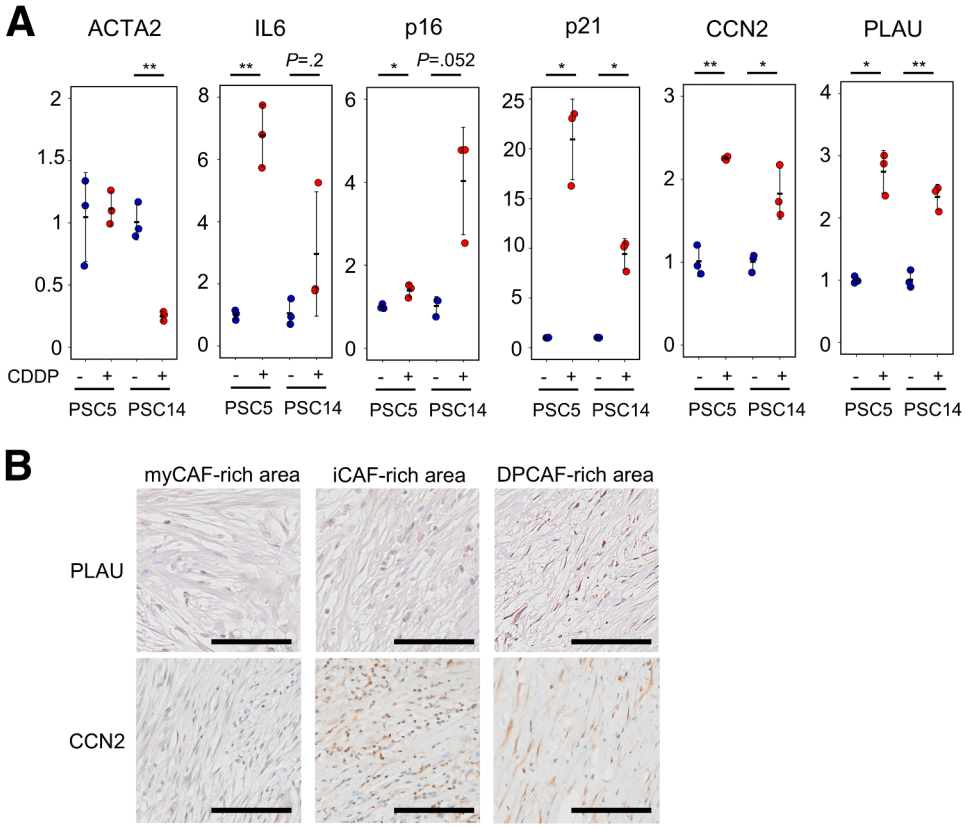


Figure 10. Gene expression analysis of senescent CAFs. (*A*) qRT-PCR analysis of human PDAC–derived CAF cell lines. RNA was extracted from PSC5 and PSC14 cells treated with and without CDDP for 7 days. (*B*) Immunohistochemical staining of PLAU and CCN2 in PDAC specimens without prior chemotherapy. Scale bars, 100 μm. Student's *t* test. $^{*}P < .05$, $^{**}P < .01$. qRT-PCR, quantitative reverse transcription polymerase chain reaction.

slide images using a Research Slide Scanner VS200 (EVIDENT) with a $\times$40 objective lens and subsequently analyzed using OLyVIA v4.1 software (EVIDENT).

Image Analysis

Whole-slide images were analyzed using ImageJ (version 1.54p). CAF-enriched regions were defined based on αSMA and IL6 double immunostaining. Whole-slide images were examined at high magnification, and each field of view was evaluated for the proportional composition of CAF subtypes. The CAF subtype representing the highest fraction within a given field was designated as the predominant CAF for that location, and the field was assigned to the corresponding CAF-enriched region. For each tumor, the tumor center and the gross tumor edge were identified on the macroscopic image and then mapped onto the corresponding whole-slide image to ensure accurate spatial alignment.

For spatial analysis, the tumor area was approximated as a circle, and radial distances from the tumor center were normalized such that the distance from the tumor center to the gross tumor edge was defined as 1. Accordingly, the tumor center was assigned a value of 0 and the gross tumor edge was assigned a value of 1. Because the specimens were resected with an adequate resection margin beyond the gross tumor edge, regions located outside the gross tumor edge were also included in the analysis and were assigned values greater than 1. These extratumoral regions exhibited pathologic features distinct from normal pancreatic tissue, and fibroblasts in these areas were operationally defined as CAFs for the purpose of spatial quantification. To quantitatively represent the 2-dimensional spatial distribution of each CAF subtype relative to the tumor center, we calculated, for each CAF population, the radius of a circle centered at the tumor center that encompassed 50 percent of the total CAF area. This radius was defined as the mean distance of the respective CAF subtype from the tumor center.

The proportion of the KRT7-positive area within each CAF subtype–enriched area was quantified as an area ratio. Collagen-positive regions identified by EVG staining were quantified as a proportion of the stromal area, which was defined as the total area of each CAF subtype–enriched region minus the KRT7-positive area. For CD8 and CD4, the number of positive cells per stromal area (cells/mm^2) was calculated. For Ki67, 3 representative high-power fields (400 μm $\times$ 400 μm) were examined for each case and each region, and the proportion of Ki67-positive cells among fibroblast-like stromal cells was determined. For quantification of p16 positivity, the image analysis software Halo (Indica Labs) was used. The software was trained using machine learning to identify spindle-shaped CAFs, enabling their

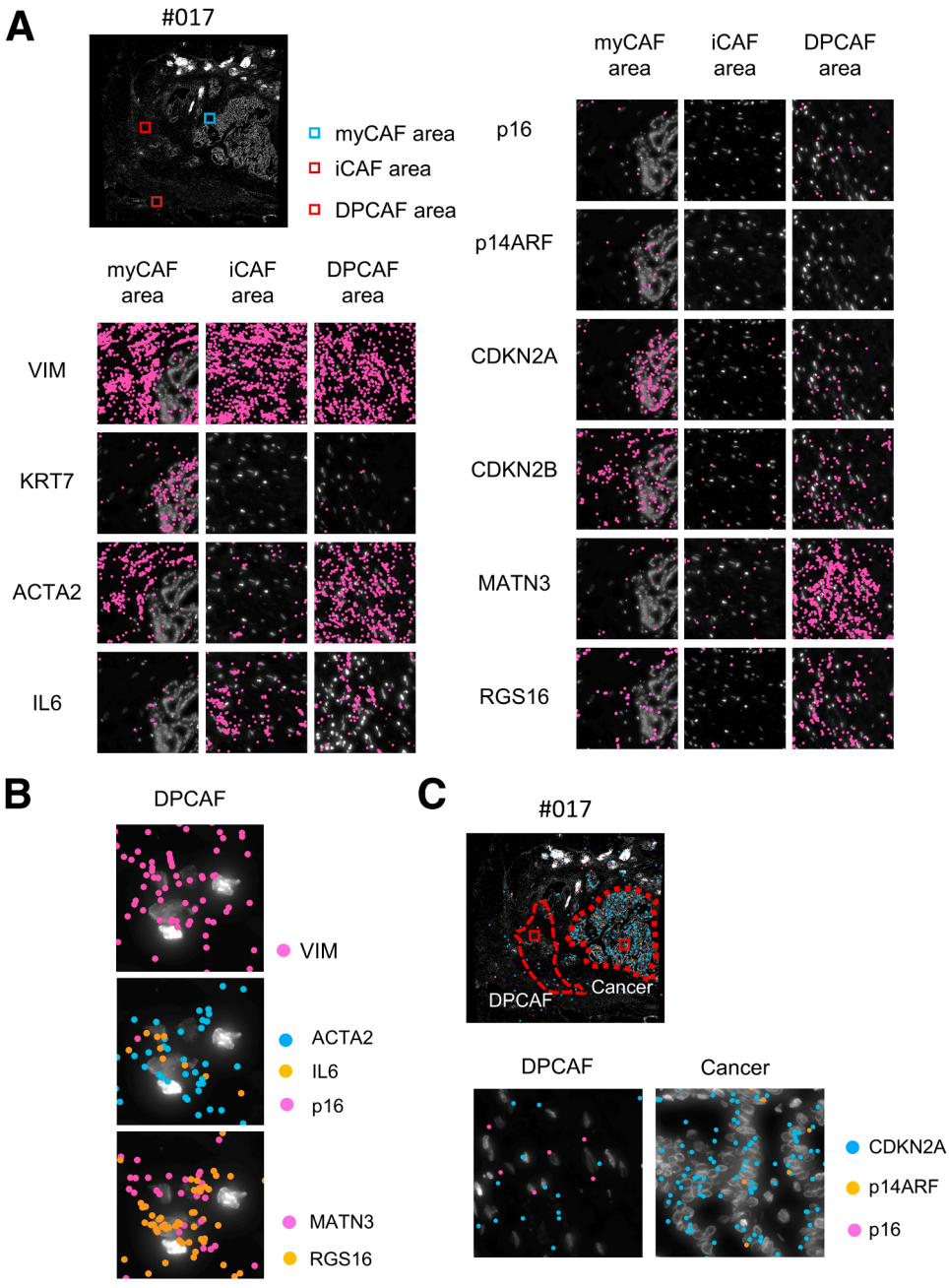


Figure 11. Subcellular-level spatial transcriptomic analysis. (*A*) Representative gene expression patterns in myCAF-, iCAF-, and DPCAF-rich areas. The locations of each CAF-rich area are indicated in the overview images, and the same regions are shown for different genes. (*B*) High-magnification view illustrating gene expression in DPCAFs. (*C*) Differences in the spatial distribution of CDKN2A, p16, and p14ARF expression between DPCAFs and cancer cells. The magnified regions shown for DPCAF-rich and cancer cell–rich areas are indicated in the overview images.

classification. The area of p16-positive CAFs was measured and divided by the total CAF area to calculate the p16 positivity rate.

Spatial Transcriptome Analysis

Spatial transcriptomic analyses were performed using Visium CytAssist and Xenium platforms (10x Genomics). Based on immunohistochemistry images, regions of interest were selected to include representative myCAF-rich, iCAF-rich, and DPCAF-rich areas. For Visium, 6.0 × 6.0 mm areas were selected, whereas for Xenium, 10 × 10 mm areas were selected for analysis. Five-micrometer-thick sections were cut from human PDAC FFPE tissue blocks and used for spatial transcriptomic profiling.

Visium sample processing was performed according to the manufacturer's instructions. Raw FASTQ files and histologic images were processed and integrated using the Space Ranger software (version 2.0.0; 10x Genomics). Downstream analyses were conducted in R (version 4.4.3) using the Seurat package (version 5.3.0). The Harmony package (version 1.2.3) was used to correct for batch effects across samples. Pseudotime analysis was performed using the Monocle3 package (version 1.3.7), and cell–cell interaction analysis was conducted with the CellChat package (version 2.1.2). Communication probabilities

between cell groups were inferred based on known ligand–receptor interactions, generating a weighted and directed signaling network in which nodes represent cell groups and edges represent inferred signaling interactions. Network roles were defined using centrality measures implemented in CellChat.[40] Sender and receiver were identified based on outgoing and incoming signaling strength, respectively, calculated as the total communication probability of signals sent to or received from other cell groups. Mediator was defined based on flow-based centrality, reflecting the extent to which a cell group lies on communication paths between other groups. Influencer was determined using a global centrality metric that quantifies the overall impact of a cell group on information flow within the signaling network. GSEA was carried out using GSEA software (version 4.3.3; Broad Institute), and pathway analysis was performed using DAVID (https://davidbioinformatics.nih.gov/home.jsp).

Xenium sample processing was performed following the manufacturer's Xenium In Situ Gene Expression with Cell Segmentation Staining User Guide. The gene panel consisted of 377 genes from the Human Multi-Tissue and Cancer Panel, supplemented with custom-selected genes. The results were visualized using the Xenium Explorer (version 3.2.0; 10x Genomics).

Cell Culture

Human pancreatic CAF cell lines hPSC-5 and hPSC-14 were obtained from RIKEN Cell Bank.[22,41] Cells were maintained in Dulbecco's Modified Eagle Medium/Ham's F-12 medium (FUJIFILM Wako Pure Chemical Corporation) supplemented with 10% fetal bovine serum. To induce cellular senescence, the cells were treated with cisplatin (FUJIFILM Wako Pure Chemical Corporation) at a concentration of 2 μg/mL for 7 days.[42]

Quantitative Reverse Transcription Polymerase Chain Reaction

Total RNA was extracted from the cells using an RNeasy Micro Kit (Qiagen) according to the manufacturer's instructions. Complementary DNA was synthesized with the PrimeScript RT Reagent Kit with gDNA Eraser (Takara Bio Inc). Quantitative reverse transcription polymerase chain reaction was carried out on a QuantStudio 5 Real-Time PCR System (Applied Biosystems) using TB Green Premix Ex Taq II (Takara Bio). Gene expression levels were normalized to β-actin as an internal control. The primer sequences were as follows: β-actin, Forward: GGACTTCGAGCAAGAGATGG, Reverse: AGCACTGTGTTGGCGTACAG; PLAU, Forward: TCCTGGTCGTGAGCGACT, Reverse: GTGACCATTCCCCTCATAGCA; ACTA2, Forward: CCACCCAGTGTGGAGCAG, Reverse: GGCAGTGCTGTCCTCTTCTT; CCN2, Forward: CTTGCGAAGCTGACCTGGAA, Reverse: CCGTCGGTACATACTCCACA.

Statistical Analysis

Statistical analyses were performed using the Mann–Whitney U test, Student's t test, χ^2 test, or Kaplan–Meier survival analysis using the R software (version 4.1.2, R Foundation for Statistical Computing) and Microsoft Office Excel (Microsoft).

Supplementary Material

Note: To access the supplementary material accompanying this article, visit the full text version at https://doi.org/10.1016/j.jcmgh.2026.101808.

References

1. Hingorani SR. Epithelial and stromal co-evolution and complicity in pancreatic cancer. Nat Rev Cancer 2023;23:57–77.
2. Kung HC, Zheng KW, Zimmerman JW, et al. The tumour microenvironment in pancreatic cancer - new clinical challenges, but more opportunities. Nat Rev Clin Oncol 2025;22:969–995.
3. Halbrook CJ, Lyssiotis CA, Pasca di Magliano M, et al. Pancreatic cancer: advances and challenges. Cell 2023;186:1729–1754.
4. Sahai E, Astsaturov I, Cukierman E, et al. A framework for advancing our understanding of cancer-associated fibroblasts. Nat Rev Cancer 2020;20:174–186.
5. Chen Y, McAndrews KM, Kalluri R. Clinical and therapeutic relevance of cancer-associated fibroblasts. Nat Rev Clin Oncol 2021;18:792–804.
6. Cheng PSW, Zaccaria M, Biffi G. Functional heterogeneity of fibroblasts in primary tumors and metastases. Trends Cancer 2025;11:135–153.
7. Özdemir BC, Pentcheva-Hoang T, Carstens JL, et al. Depletion of carcinoma-associated fibroblasts and fibrosis induces immunosuppression and accelerates pancreas cancer with reduced survival. Cancer Cell 2014;25:719–734.
8. Rhim AD, Oberstein PE, Thomas DH, et al. Stromal elements act to restrain, rather than support, pancreatic ductal adenocarcinoma. Cancer Cell 2014;25:735–747.
9. Lee JJ, Perera RM, Wang H, et al. Stromal response to Hedgehog signaling restrains pancreatic cancer progression. Proc Natl Acad Sci U S A 2014;111:E3091–E3100.
10. Lavie D, Ben-Shmuel A, Erez N, et al. Cancer-associated fibroblasts in the single-cell era. Nat Cancer 2022;3:793–807.
11. Öhlund D, Handly-Santana A, Biffi G, et al. Distinct populations of inflammatory fibroblasts and myofibroblasts in pancreatic cancer. J Exp Med 2017;214:579–596.
12. Biffi G, Oni TE, Spielman B, et al. IL1-induced JAK/STAT signaling is antagonized by TGFβ to shape CAF heterogeneity in pancreatic ductal adenocarcinoma. Cancer Discov 2019;9:282–301.
13. Ogrodnik M, Carlos Acosta J, Adams PD, et al. Guidelines for minimal information on cellular senescence experimentation in vivo. Cell 2024;187:4150–4175.
14. Ferreira-Gonzalez S, Matsumoto T, Hara E, et al. Senescence, aging and disease throughout the

gastrointestinal system. Gastroenterology 2025; 169:1357–1379.
15. Faget DV, Ren Q, Stewart SA. Unmasking senescence: context-dependent effects of SASP in cancer. Nat Rev Cancer 2019;19:439–453.
16. Yoshimoto S, Loo TM, Atarashi K, et al. Obesity-induced gut microbial metabolite promotes liver cancer through senescence secretome. Nature 2013;499:97–101.
17. Okumura S, Konishi Y, Narukawa M, et al. Gut bacteria identified in colorectal cancer patients promote tumourigenesis via butyrate secretion. Nat Commun 2021;12:5674.
18. Wang T, Notta F, Navab R, et al. Senescent carcinoma-associated fibroblasts upregulate IL8 to enhance prometastatic phenotypes. Mol Cancer Res 2017; 15:3–14.
19. Belle JI, Sen D, Baer JM, et al. Senescence defines a distinct subset of myofibroblasts that orchestrates immunosuppression in pancreatic cancer. Cancer Discov 2024;14:1324–1355.
20. Liu L, Huang H, Cheng B, et al. Revealing the role of cancer-associated fibroblast senescence in prognosis and immune landscape in pancreatic cancer. iScience 2025;28:111612.
21. Assouline B, Kahn R, Hodali L, et al. Senescent cancer-associated fibroblasts in pancreatic adenocarcinoma restrict CD8. Nat Commun 2024;15:6162.
22. Takikawa T, Hamada S, Matsumoto R, et al. Senescent human pancreatic stellate cells secrete CXCR2 agonist CXCLs to promote proliferation and migration of human pancreatic cancer AsPC-1 and MIAPaCa-2 cell lines. Int J Mol Sci 2022;23:9275.
23. Childs BG, Gluscevic M, Baker DJ, et al. Senescent cells: an emerging target for diseases of ageing. Nat Rev Drug Discov 2017;16:718–735.
24. Schmitt CA, Wang B, Demaria M. Senescence and cancer - role and therapeutic opportunities. Nat Rev Clin Oncol 2022;19:619–636.
25. Wang L, Lankhorst L, Bernards R. Exploiting senescence for the treatment of cancer. Nat Rev Cancer 2022; 22:340–355.
26. Ye J, Melam A, Stewart SA. Stromal senescence contributes to age-related increases in cancer. Nat Rev Cancer 2025;25:781–800.
27. Golesworthy B, Wang Y, Tanti A, et al. Intra-tumoral CD8+ T-cell infiltration and PD-L1 positivity in homologous recombination deficient pancreatic ductal adenocarcinoma. Front Oncol 2022;12:860767.
28. Blando J, Sharma A, Higa MG, et al. Comparison of immune infiltrates in melanoma and pancreatic cancer highlights VISTA as a potential target in pancreatic cancer. Proc Natl Acad Sci U S A 2019; 116:1692–1697.
29. Suryadevara V, Hudgins AD, Rajesh A, et al. SenNet recommendations for detecting senescent cells in different tissues. Nat Rev Mol Cell Biol 2024; 25:1001–1023.
30. Fridman AL, Tainsky MA. Critical pathways in cellular senescence and immortalization revealed by gene expression profiling. Oncogene 2008;27:5975–5987.
31. Hannon GJ, Beach D. p15INK4B is a potential effector of TGF-beta-induced cell cycle arrest. Nature 1994; 371:257–261.
32. Leask A, Abraham DJ. TGF-beta signaling and the fibrotic response. FASEB J 2004;18:816–827.
33. Santibanez JF, Krstic J. Transforming growth factor-beta and urokinase type plasminogen interplay in cancer. Curr Protein Pept Sci 2018;19:1155–1163.
34. Shen YW, Zhou YD, Chen HZ, et al. Targeting CTGF in cancer: an emerging therapeutic opportunity. Trends Cancer 2021;7:511–524.
35. Chijimatsu R, Kobayashi S, Takeda Y, et al. Establishment of a reference single-cell RNA sequencing dataset for human pancreatic adenocarcinoma. iScience 2022; 25:104659.
36. Elyada E, Bolisetty M, Laise P, et al. Cross-species single-cell analysis of pancreatic ductal adenocarcinoma reveals antigen-presenting cancer-associated fibroblasts. Cancer Discov 2019;9:1102–1123.
37. Huang H, Wang Z, Zhang Y, et al. Mesothelial cell-derived antigen-presenting cancer-associated fibroblasts induce expansion of regulatory T cells in pancreatic cancer. Cancer Cell 2022;40:656–673.e7.
38. Mizutani Y, Kobayashi H, Iida T, et al. Meflin-positive cancer-associated fibroblasts inhibit pancreatic carcinogenesis. Cancer Res 2019;79:5367–5381.
39. Neuzillet C, Nicolle R, Raffenne J, et al. Periostin- and podoplanin-positive cancer-associated fibroblast subtypes cooperate to shape the inflamed tumor microenvironment in aggressive pancreatic adenocarcinoma. J Pathol 2022;258:408–425.
40. Jin S, Plikus MV, Nie Q. CellChat for systematic analysis of cell-cell communication from single-cell transcriptomics. Nat Protoc 2025;20:180–219.
41. Masamune A, Kikuta K, Watanabe T, et al. Fibrinogen induces cytokine and collagen production in pancreatic stellate cells. Gut 2009;58:550–559.
42. Hayashi K, Horisaka K, Harada Y, et al. Polyploidy mitigates the impact of DNA damage while simultaneously bearing its burden. Cell Death Discov 2024;10:436.

Received November 30, 2025. Accepted May 5, 2026.

Correspondence
Address correspondence to: Tomonori Matsumoto, MD, PhD, Laboratory of Ploidy Pathology, Graduate School of Frontier Biosciences, The University of Osaka, 1-3 Yamadaoka, Suita, Osaka 565-0871, Japan. e-mail: matsumoto.tomonori.fbs@osaka-u.ac.jp; or Eiji Hara, PhD, Department of Molecular Biology, Research Institute for Microbial Diseases, The University of Osaka, 3-1 Yamadaoka, Suita, Osaka 565-0871, Japan. e-mail: ehara@biken.osaka-u.ac.jp.

Acknowledgments
The authors acknowledge the NGS core facility at the Research Institute for Microbial Diseases of The University of Osaka for the spatial transcriptomic analysis. The authors are grateful to Eleanor Cook for carefully editing the English of this manuscript.

CRediT Authorship Contributions
Yoshiyuki Harada (Investigation: Lead; Writing – original draft: Equal)
Atsuhiro Masuda (Data curation: Equal; Writing – review & editing: Supporting)
Takanori Matsuura (Investigation: Supporting; Writing – review & editing: Supporting)
Kenji Nagata (Investigation: Supporting; Writing – review & editing: Supporting)
Yoshihide Nanno (Investigation: Supporting; Writing – review & editing: Supporting)

Atsushi Masamune (Investigation: Supporting; Writing – review & editing: Supporting)
Yuzo Kodama (Investigation: Supporting; Writing – review & editing: Supporting)
Eiji Hara (Conceptualization: Equal; Funding acquisition: Lead; Writing – review & editing: Lead)
Tomonori Matsumoto, MD, PhD (Conceptualization: Lead; Funding acquisition: Supporting; Writing – original draft: Lead; Writing – review & editing: Lead)

Conflicts of interest
The authors disclose no conflicts.

Funding
This work was supported by the Japan Agency for Medical Research and Development (Grant Number JP25gm1710004h0002 and 25zf0127008h0002), Japan Science and Technology Agency (Grant Number JPMJFR2212 and JPMJMS2022), and Japan Society for Promotion Science (Grant Number JP25H00443).

Data Availability
The spatial transcriptome data generated in this study have been deposited in the DDBJ Sequence Read Archive (https://www.ddbj.nig.ac.jp) under accession number PRJDB39625 and PRJDB39739. The authors declare that all other data are available upon request.